Journal of Power Sources 615 (2024) 235036

Contents lists available at ScienceDirect

Journal of Power Sources

journal homepage: www.elsevier.com/locate/jpowsour

Operando determination of lithium-ion cell temperature based on electrochemical impedance features

Tobias Hackmann [a,b,*], Sebastian Esser [c], Michael A. Danzer [b,d]

[a] BMW M GmbH, BMW Group, 80809 Munich, Germany
[b] University of Bayreuth, Chair of Electrical Energy Systems (EES), Universitätsstraße 30, 95447 Bayreuth, Germany
[c] University of Stuttgart, Department of Electrical Engineering, Pfaffenwaldring 47, 70569 Stuttgart, Germany
[d] Bavarian Center for Battery Technology (BayBatt), Universitätsstraße 30, 95447 Bayreuth, Germany

GRAPHICAL ABSTRACT

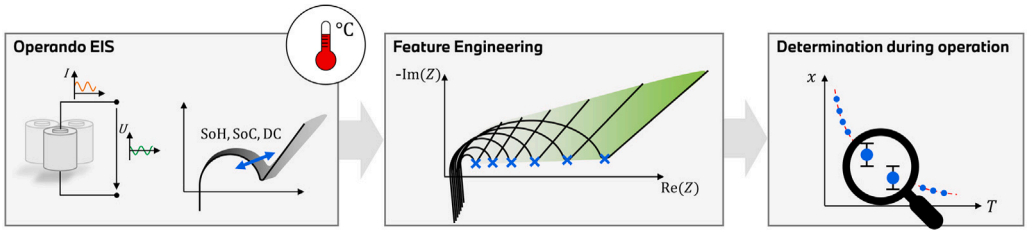

HIGHLIGHTS

- Novel method for impedance feature selection based on utility index.
- Temperature determination for different cells and states, even during operation.
- 143 established and novel features extracted from each impedance spectrum.
- Comprehensive literature review of impedance-based temperature estimation methods.
- Method can also be used for state of charge and state of health estimation.

ARTICLE INFO

Keywords:
Electrochemical impedance spectroscopy (EIS)
Non-stationarity
Temperature determination
Feature engineering
Lithium-ion battery

ABSTRACT

Electrochemical impedance spectroscopy is applied to lithium-ion batteries during operation with the general purpose of an operando characterization and specifically for battery state estimation. For the first time, 143 features of the measured impedance spectra are extracted and form the data basis that contains information on the cell states and their complex dependencies. Spectra are collected in stationary and transient conditions at varying temperatures, states of charge and states of health. A novel method is presented that enables an evaluation of features under these multidimensional dependencies. By a rigorous classification, interpretation and discussion an enhanced understanding of state dependencies and sensitivities towards operating conditions is reached. Ultimately, the selected impedance features are utilized for an operando state estimation and especially the determination of the cell internal temperature. A detailed literature review of impedance-based temperature estimation is provided. Results are presented for a Molicel INR-21700-P42A and a Samsung INR-21700-50E with an accuracy of 2 K for a wide range of operating conditions and even with increased aging.

* Corresponding author at: University of Bayreuth, Chair of Electrical Energy Systems (EES), Universitätsstraße 30, 95447 Bayreuth, Germany.
E-mail address: Tobias.HA.Hackmann@bmw-m.com (T. Hackmann).

https://doi.org/10.1016/j.jpowsour.2024.235036
Received 22 April 2024; Received in revised form 26 June 2024; Accepted 7 July 2024
Available online 25 July 2024

Nomenclature

Abbreviations

BMS	Battery management system
CC	Constant current
CH	Charge
CCCV	Constant current, constant voltage
CPE	Constant phase element
DC	Direct current
DCH	Discharge
DEIS	Dynamic electrochemical impedance spectroscopy
ECM	Equivalent circuit model
EIS	Electrochemical impedance spectroscopy
LCO	Lithium cobalt oxide
NCA	Nickel cobalt aluminum oxide
SEIS	Stationary electrochemical impedance spectroscopy
SEI	Solid electrolyte interphase
SiOx	Silicon oxide
SoC	State of charge
SoH	State of health
SoH_C	State of health with respect to capacity fade
SVR	Support vector regression
UI	Utility index

Indices

G	Superset identification variable
imag	Imaginary part of impedance
iK	ith element of group K
IR	Intersection Resistance
K	Subset identification variable
$K-$	Previous value in group K
$K+$	Subsequent value in group K
locMin	Local minimum of the locus
locMax	Local maximum of the locus
mag	Magnitude of impedance
pha	Phase of impedance
real	Real part of impedance

Parameters and Variables

A	Pre-exponential factor of Arrhenius equation
B	Offset factor of Arrhenius equation
d	Pairwise distance
$\bar{d}$	Mean of pairwise distances
$\tilde{d}$	Median of pairwise distances
d_{Min}	Minimum of pairwise distances
d_{Max}	Maximum of pairwise distances
d_{Ratio}	Ratio between minimum d_{min} and maximum d_{max}
E_a	Activation energy
f	Frequency
f_{min}	Lowest measured frequency
f_{max}	Highest measured frequency
i_{UI}	Utility index
$i_{\mathrm{UI},1\sigma}$	Utility index based on 1 σ sensitivity range
$i_{\mathrm{UI},2\sigma}$	Utility index based on 2 σ sensitivity range
l_{arc}	Length of the locus curve
L	Inductance
n	Exponent of CPE element
n_K	Number of data included in group K
n_G	Number of data included in group G
Q_{CPE}	Capacity of CPE element
R	Resistance
R_0	Effective resistance
R_c	Universal gas constant
R_d	Range of pairwise distances
T_{res}	Temperature resolution
ΔT	Temperature step size
x	Feature data
$\Delta\bar{x}$	Change in mean value
$\tilde{x}_{0.25}$	25 % quartile of measurement points
$\tilde{x}_{0.75}$	75 % quartile of measurement points
$\tilde{x}_{\mathrm{IQR}}$	Interquartile range of measurement points
Z	Impedance
Z_{R0}	Impedance of resistance R_0
Z_{L0}	Impedance of inductance
Z_{RL}	Impedance of RL element
Z_{RQ}	Impedance of ZARC element
α	Angle that encloses a straight line from $Z(f_{\mathrm{min}})$ to $Z(f_{\mathrm{max}})$ with the real axis
β_1	Angle that encloses a straight line from Z_{IR} to $Z(f_{\mathrm{min}})$ with the real axis
β_2	Angle that encloses a straight line from Z_{IR} to the local minimum (Z_{locmin}) with the real axis
β_3	Angle that encloses a straight line from Z_{IR} to the local maximum (Z_{locmax}) with the real axis
σ	Standard deviation
$\Delta\sigma_K$	Change in standard deviation of group K
σ_d^2	Variance of pairwise distances
ω	Angular velocity

1. Introduction

Monitoring lithium-ion batteries is crucial for their operation, performance, lifespan, and safety in automotive applications. The battery management system (BMS) is responsible for ensuring that the operating limits of the cells are maintained. The BMS relies on acquiring measurement data and utilizing simulation models to predict the condition of cells. This is necessary as certain operating states, such as state of charge (SoC) or state of health (SoH), cannot be measured directly [1].

Research in cell analysis emphasizes a new technological approach — electrochemical impedance spectroscopy (EIS). Laboratory tests have demonstrated that this technology has great potential. Due to the good correlation between the change in temperature [2–4], SoC [5,6], SoH [7–9] and the measured impedance, as well as the fact that it enables these parameters to be determined simultaneously, the online capability of this method is increasingly being investigated, cf. [10]. However, to achieve a valid and reproducible state estimation using this technology, it is necessary to understand and compensate for the influences on the impedance or take them into account during the measurement [11]. Such measures are especially important if the EIS needs to be conducted during operation.

Raijmakers et al. uses the EIS to measure the internal cell temperature [2]. The point of intersection with the real axis in the Nyquist diagram is used as a feature, which is called the characteristic frequency f_0 [2]. It is independent of the state of charge, but is strongly dependent on the temperature [2]. The associated ohmic resistance is also independent of the SoC [12]. With increasing temperature, this value decreases mainly due to the electrolyte's conductivity [12]. Spinner et al. found that the assumption of SoC independence in the high frequency range is only valid if a stable solid electrolyte interface (SEI) is present [13]. The authors note that this changes significantly with an increase in temperature (65 °C < T < 100 °C). However, the described SoC independence in the high frequency range can also be influenced by inductances, which are affected by the cables of the measuring device, the cell geometry and the windings [14–16]. As these parameters do not change with varying cell states, the inductance is predicted to be independent of temperature and SoC [2].

The above explanations suggest that the interpretation of impedance spectrum results can be influenced by a number of factors that depend on the measurement setup as well as cell chemistry and cell states. These complex interactions explain why different research groups have relied on various features for temperature estimation, as shown in Table A.1 in the appendix. The literature mainly uses features from the raw data, such as magnitude and phase or real and imaginary parts at discrete frequencies. In addition to this widespread approach, some research groups extract features based on a model. They approximate the impedance spectrum with an equivalent electrical circuit and analyze the values of individual elements via temperature change [3,17,18]. Additionally, there are publications that base temperature estimation on several features, rather than just individual characteristics. Beelen et al. optimized the weighting of the real and imaginary parts to improve temperature estimation [19,20]. Recently, more data-based methods have been employed. Ströbel et al. used artificial neural networks to ensure precise temperature estimation even under varying conditions [21,22]. Ouyang et al. also used machine learning algorithms, but focused on support vector regression (SVR) [6]. They trained the algorithm using a reduced number of features. The suitability of a feature is typically evaluated using a regression analysis with an n^{th}-order polynomial [13,23–26] or the Arrhenius equation [2,13,27–30]. Individual features for machine learning algorithms are selected using the Pearson correlation [6].

This article presents a novel method for evaluating features from the impedance spectrum to determine temperature, even when cell states such as SoH or SoC change. The multidimensional dependencies are characterized by a figure of merit — the so-called utility index (UI). It is used to give a recommendation for the selection of features. Due to the underlying calculation method, it is possible to predict achievable accuracies. For the first time, 143 features of the impedance spectrum are extracted for further analysis. Already known features from literature are also compared with new approaches. To demonstrate this method, battery states such as SoH, SoC, temperature, and C-rate are varied. The methodology is presented with a focus on temperature determination. Due to its general approach, it can also be used for SoC and SoH estimation.

2. Methodology

The methodology is based on the basic principles of applied machine learning [31], which is why the following sections can be subdivided into Feature Extraction and Feature Selection.

2.1. Impedance feature extraction

Features are extracted from the measured impedance spectra, which can be evaluated with regard to their sensitivity for temperature determination. For this purpose, a total of 143 features are generated from each impedance spectrum using four different approaches: raw data, geometry, equivalent circuit model (ECM) and statistics.

2.1.1. Features from raw data

Temperature estimation is most commonly achieved through the use of features extracted from raw data, see Table A.1. In literature, authors typically utilize only the Cartesian coordinates (real and imaginary parts) or the polar coordinates (magnitude and phase) of the impedance, with few exceptions. These values can be measured and calculated for each frequency point, resulting in a variety of characteristics published in the literature. This variation can also be attributed to the influence of different cell states and external conditions. To analyze the entire impedance spectrum without increasing the number of features unnecessarily, 15 frequencies are distributed logarithmically across a frequency range between f_{min} and f_{max}. This approach provides a comprehensive representation of the entire spectrum. Discretization is permissible because influences always affect an impedance range and not individual frequencies, provided there is no influence from interference or other inductive effects. It is important to consider this simplification when interpreting the results.

2.1.2. Geometry

The geometry category comprises impedance features that are not associated with a specific frequency but are derived from the locus of the impedance spectrum by considering multiple frequency support points. The features are listed in the following Table 1.

Table 1
List of features from geometry.

Name	Description
Z_{IR}	Impedance at intersection with real axis
f_{IR}	Intersection frequency
α	Angle that encloses a straight line from $Z(f_{\mathrm{min}})$ to $Z(f_{\mathrm{max}})$ with the real axis
β_1	Angle that encloses a straight line from Z_{IR} to $Z(f_{\mathrm{min}})$ with the real axis
β_2	Angle that encloses a straight line from Z_{IR} to the local minimum (Z_{locmin}) with the real axis
β_3	Angle that encloses a straight line from Z_{IR} to the local maximum (Z_{locmax}) with the real axis
l_{arc}	Length of the locus curve
Z_{locMin}	Local minimum of the locus, cf. Fig. 1
Z_{locMax}	Local maximum of the locus, cf. Fig. 1
$d_{\mathrm{IR,\ locMin}}$	Distance between Z_{IR} and Z_{locmin}
$d_{\mathrm{IR,\ locMax}}$	Distance between Z_{IR} and Z_{locmax}

The intersection of the impedance spectrum with the real axis in the Nyquist plot is a useful indicator for estimating temperature, see Table A.1. To obtain the most accurate zero crossing Z_{IR}, a linear interpolation is performed due to the discrete frequency support points. The corresponding intersection frequency f_{IR} is then approximated based on this value. Additional angular relationships (α, β_{1-3}) were added to analyze changes in the entire locus curve. The selection is based on an exploratory data analysis, which revealed a correlation with changes in temperature. The same correlation was observed for the length of the locus curve l_{arc}, as well as for the local maxima Z_{locMax} and minima Z_{locMin}. For the latter two, the real and imaginary parts were evaluated separately.

2.1.3. ECM

Cell impedance spectra can be approximated using an equivalent circuit model. As the use of an ECM is very common in literature, the implementation is only described roughly, but can be found in more detail in [32–34]. The following Fig. 1 illustrates the ECM network used and presents a result based on the Samsung SDI INR-21700-50E (SDI50E) measurement series as an example, cf. Table 3.

Effective resistance R_0 is used to describe the electrical and ionic conductivity. It can be interpreted as the sum of ohmic resistances (electrolyte, active material, current collector, ...) [10,35,36], where the electrolyte conductivity is the determining factor [37]. It does not

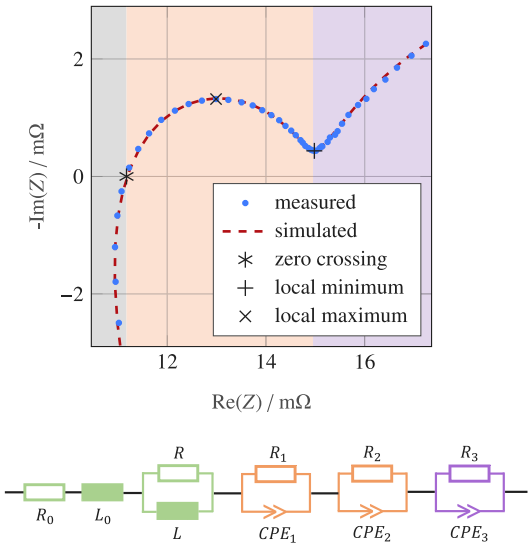

Fig. 1. Illustration of an impedance spectrum from the SDI50E measurement series at: SoH = 100 %, SoC = 10 %, T = 25 °C, DC = 0 A. In addition, the approximated spectrum and the equivalent electrical circuit configuration used are shown.

lead to any change in the phase relationship and is therefore frequency independent and purely real:

$$Z_{\mathrm{R0}}(j\omega) = R_0. \tag{1}$$

As mentioned in the introduction, cabling and cell winding can affect the impedance. The series inductance

$$Z_{\mathrm{L0}}(j\omega) = j\omega L_0 \tag{2}$$

and the parallel connection of resistance and inductance

$$Z_{\mathrm{RL}}(j\omega) = \frac{j\omega L}{1 + \frac{j\omega L}{R}} \tag{3}$$

were used for this purpose. However, most of the impedance spectrum is dominated by resistive–capacitive processes. Since the battery cell consists of two electrodes and thus has at least two dominant time constants, two ZARC elements were also used for this purpose, see Fig. 1. Such an element can be formed by connecting a resistor and a constant phase element (CPE) in parallel. Its mathematical definition is given by

$$Z_{\mathrm{RQ}}(j\omega) = \frac{R}{R \cdot Q_{\mathrm{CPE}} \cdot (j\omega)^n + 1}, \quad 0 \le n \le 1. \tag{4}$$

In addition, another ZARC element is used to describe the low frequency behavior. It allows a simplified representation of the diffusion path. The total impedance

$$Z(j\omega) = R_0 + L_0 + Z_{\mathrm{RL}}(j\omega) + Z_{\mathrm{RQ1}}(j\omega) + Z_{\mathrm{RQ2}}(j\omega) + Z_{\mathrm{RQ3}}(j\omega) \tag{5}$$

results from the series connection of the individual elements. Taking the above Eqs. (1)–(5) into account, the total impedance consists of 13 variables, which are summarized in Table D.1. To solve equation (5) approximately, the non-linear least squares method is used. The Matlab solver "lsqnonlin" attempts to minimize the resulting residuals with respect to the target values over the entire impedance spectrum.

2.1.4. Statistics

Statistical methods are intended to provide information on the distribution, variation and tendency of the measured values. Table 2 presents the selected statistical features. Real and imaginary parts as well as magnitude and phase are evaluated individually.

Some of the features require the calculation of the pairwise distance. The Euclidean distance is chosen for this, as it can be used to describe

Table 2
List of features from Statistics.

Name	Description
d_{Min}	Minimum of pairwise distances
d_{Max}	Maximum of pairwise distances
d_{Ratio}	Ratio between minimum d_{min} and maximum d_{max}
$\bar{d}$	Mean of pairwise distances
$\tilde{d}$	Median of pairwise distances
σ_{d}^2	Variance of pairwise distances
R_{d}	Range of pairwise distances
$\tilde{x}_{0.25}$	25 % quartile of measurement points
$\tilde{x}_{0.75}$	75 % quartile of measurement points
$\tilde{x}_{\mathrm{IQR}}$	Interquartile range of measurement points

the relationship between two points in two-dimensional space [38, p.15]. If this calculation is performed for all frequencies, the distance between each measurement point and all others can be determined. The application to the real and imaginary parts is permissible, as they have a common reference system and the same unit. This does not apply to magnitude and phase, so the pairwise distance is calculated individually. In the following, the distance matrix can be used to apply statistical methods. The minimum value d_{min}, maximum value d_{max} or the ratio of both to each other d_{ratio} is formed. This allows a statement to be made regarding the range as well as outliers and inconsistencies. The mean $\bar{d}$ and median $\tilde{d}$ can be used to illustrate the overall trend. However, the latter is less sensitive to outliers [39, p. 77]. The first and third quartile ($\tilde{x}_{0.25}$, $\tilde{x}_{0.75}$) represent the value below which 25 % and 75 % of the data are located. Together with the range R_{d}, interquartile range $\tilde{x}_{\mathrm{IQR}}$ and the variance σ_{d}^2, they serve as an indicator for the dispersion of the data [39].

2.2. Impedance feature selection — utility index

The pre-processed data from Section 2.1 is used for classification based on common cell states. The correct allocation to the individual groups is of great importance for the further calculation. It can be useful to work with fixed threshold values in order to be able to better control the classification, especially with small amounts of data. Within a group K the cell states are constant, only the values of the associated feature x_{iK} differ. As already mentioned, a sufficient amount of data, but at least 3 values per group, is required to achieve a useful statistical distribution. The mean value

$$\bar{x}_K = \frac{1}{n_K} \cdot \sum_{i=1}^{n_K} x_{iK} \tag{6}$$

and the associated standard deviation

$$\sigma_K = \sqrt{\frac{1}{n_K} \cdot \sum_{i=1}^{n_K} (x_{iK} - \bar{x}_K)^2} \tag{7}$$

are calculated individually for each group K, where n_K is the number of data contained. The data obtained in this way can be summarized over the various temperatures to form a superset G, so that $K \subseteq G$ applies. It leads to a classification of the same cell states over temperature. An example of this can be seen in Fig. 2(a). The group assignment can be recognized by the color scaling, where a subdivision takes place exclusively based on the SoC. For better readability, each $\bar{x}_K$ of the subset K is labeled with the corresponding temperature.

The classification allows the calculation of the group-specific utility index $i_{\mathrm{UI},K}$, which is explained in more detail below. It is introduced to obtain a global measure for analyzing the usefulness of a feature. To ensure comparability across all units of measurement, the UI is a dimensionless quantity. The calculation is based on the ratio of the standard deviation σ_K to the change in the mean value $\Delta\bar{x}_K$, normalized to 1. This is a modification of the coefficient of variation, which uses

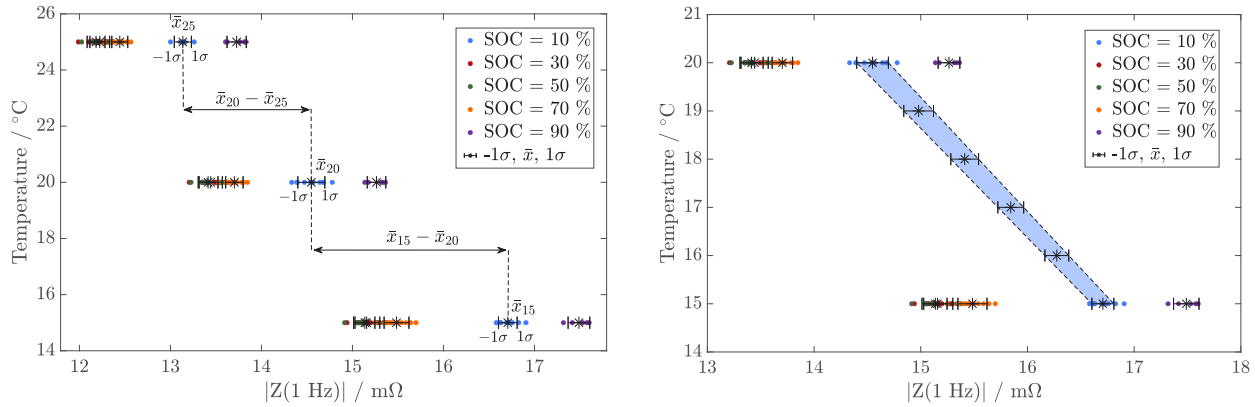

Fig. 2. Illustration of the utility index calculation methodology. Both diagrams refer to the stationary EIS data of the MoliP42 A measurement series. The magnitude at 1 Hz ($|Z(1\ \text{Hz})|$) was used as an example. (a) shows the calculation based on the sensitivities of the respective temperature reference. (b) illustrates the interpolation approach for calculating the UI based on a given temperature difference.

the change in the mean value over temperature for calculation. For equidistant temperatures it is defined as:

$$i_{\text{UI}}(\sigma, \Delta\bar{x}) = 1 - \frac{\sigma}{|\Delta\bar{x}|}. \tag{8}$$

The utility index is calculated individually for each group K, but results from the mean value of two UIs. They arise due to different values for $\Delta\bar{x}_K$. For the calculation, the change in the mean value to the next higher $\Delta\bar{x}_{K+}$ and lower temperature $\Delta\bar{x}_{K-}$ is evaluated. An example of this can be seen in Fig. 2(a). The index $i_{\text{UI},K}$ can therefore be calculated using

$$i_{\text{UI},K} = \frac{i_{\text{UI}}(\sigma_K, \Delta\bar{x}_{K+}) + i_{\text{UI}}(\sigma_K, \Delta\bar{x}_{K-})}{2} \tag{9}$$

for each group K. Eq. (8) is restricted to equidistant temperatures, therefore it is extended through linear interpolation (see blue shaded area in Fig. 2(b)). This ensures a common calculation basis within group G, and prevents different weightings. Additionally, it allows for sensitivity adjustments. For this purpose, the variable T_{res} is introduced, which specifies the desired temperature resolution. Interpolation is performed between mean values and standard deviations. This results in

$$i_{\text{UI},K}(\sigma_K, \Delta\bar{x}_K, \Delta\sigma_K, \Delta T_K) = 1 - \frac{\sigma_K - (\Delta\sigma_K - \frac{\Delta\sigma_K}{\Delta T_K} \cdot T_{\text{res}})}{|\frac{\Delta\bar{x}_K}{\Delta T_K} \cdot T_{\text{res}}|}. \tag{10}$$

The two-sided approach σ_{K+}, σ_{K-} applies to both the change in the mean value and the change in the standard deviation. Eq. (9) takes this into account. Based on Eq. (8), the following limit consideration results for the utility index:

$$\begin{aligned} &\lim_{\sigma\to 0} \ i_{\text{UI}}(\sigma, \Delta\bar{x}) = 1 && \lim_{\Delta\bar{x}\to 0^+} \ i_{\text{UI}}(\sigma, \Delta\bar{x}) = -\infty \\ &\lim_{\sigma\to +\infty} \ i_{\text{UI}}(\sigma, \Delta\bar{x}) = -\infty && \lim_{\Delta\bar{x}\to 0^-} \ i_{\text{UI}}(\sigma, \Delta\bar{x}) = -\infty \\ & && \lim_{\Delta\bar{x}\to -\infty} \ i_{\text{UI}}(\sigma, \Delta\bar{x}) = 1 \\ & && \lim_{\Delta\bar{x}\to +\infty} \ i_{\text{UI}}(\sigma, \Delta\bar{x}) = 1 \end{aligned}$$

It should be noted that $\sigma \in \mathbb{R}^+$ and $\Delta\bar{x} \in \mathbb{R}^*$. The following also applies to the domain $\mathbb{D}_{\text{UI}}$ of the utility index: $\mathbb{D}_{\text{UI}} = \{i_{\text{UI}} \mid i_{\text{UI}} \in \mathbb{R}_0^+, 0 \le i_{\text{UI}} \le 1\}$, whereby negative values are set to 0. The explanations above can be interpreted as follows: If the standard deviation is greater than or equal to the change in the mean value, the UI converges to 0. Conversely, it approaches 1 when the distance between the two values becomes maximum.

By introducing the utility index and using Eqs. (9) and (10), an associated $i_{\text{UI},K}$ is obtained for each feature x of a group K. The arithmetic mean is then used to calculate a single value

$$i_{\text{UI},G} = \frac{1}{n_G} \cdot \sum_{i=1}^{n_G} i_{\text{UI},iK} \tag{11}$$

that represents the usefulness of a feature within the superset G from a number n_G of corresponding indices.

The analysis of $i_{\text{UI},G}$ enables the selection of one or more appropriate features. The highest potential for reproducible and precise estimation of the target variable, temperature in this case, is assigned to the maximum across all index values. A detailed analysis based on different temperature ranges is also possible, depending on the definition of group G, see Section 4.3. Additionally, the utility index can be calculated by combining the groups G into a common superset, for example, across all states of charge and states of health. The calculation is similar to Eq. (11).

3. Experiments

3.1. Measurement setup

To analyze the various cell states and their resulting influences using the developed methodology, a comprehensive cell measurement is required. For this purpose, two independent measurement series were conducted on two different cells: the MoliP42 A and the SDI50E. The specifications for each individual cell can be found in Table 3.

Table 3
Cell specification. The Molicel INR-21700-P42A data is obtained from an internal teardown report. Unless otherwise stated, the data for the SDI INR-21700-50E is taken from [40].

	Molicel INR-21700-P42A	Samsung SDI INR-21700-50E
format:	21 700	21 700
nominal capacity:	4.20 Ah	4.90 Ah
nominal voltage:	3.6 V	3.63 V
operating range:	2,5 – 4,2 V	2,5 – 4,2 V [41]
chemistry:	NCA | C + SiOx	NCA | C + Si

The cells are evaluated using different equipment on separate test benches. Each setup ensures good contact and minimal external magnetic field interference, achieved through the use of spring contact pins, Kelvin contacting, and twisted sense lines. Galvanostatic excitation is chosen for the EIS measurement, utilizing a Gamry galvanostat and the EIS option of the SL1132 A test bench. The systems and measurement setup are listed in Table 4.

The excitation amplitude is selected so that linearity is maintained and a high signal to noise ratio is achieved.

Table 4
Measurement setup.

	Molicel INR-21700-P42A	Samsung SDI INR-21700-50E
Battery cell tester:	Scienlab SL1132A	Scienlab SL6/30/0.18BTS20C
Cell contacting:	spring probe pins, kelvin-connection	spring probe pins, kelvin-connection
Temperature sensor:	PT1000	PT100
EIS – specification		
Equipment:	cell tester	Gamry Interface 5000
Frequency range:	5 kHz–50 mHz, 51 points	10 kHz–100 mHz, 51 points
Amplitude:	300 mA	250 mA

3.2. Measurement procedure

Due to the objectives of both measurement series, the test procedures differ, see Table 5. The SDI50E measurement series focuses on a comprehensive variation of important cell states. To achieve this, a cyclic ageing campaign is initiated. For each SoH, see Table 5, three cells undergo a 0.5 C constant current, constant voltage (CCCV) charge cycle, followed by a 1 C discharge profile at 30 °C. After four standard cycles, two additional fast charge profiles with a maximum C-rate of 2.25 C are inserted. Upon reaching the specified remaining capacity, the cells are subjected to the EIS characterization process, which is illustrated in the flow chart in Fig. B.1b. The measurement process begins by setting the climate chamber temperature and allowing sufficient time for temperature distribution to become homogeneous inside the cells. Subsequently, the cells are charged with the CCCV profile up to the cut-off voltage. Once the termination condition is met, the batteries are discharged to the desired state of charge using constant current and Coulomb counting. In order to prevent accelerated aging and interruption caused by the superimposed constant currents, the edge areas of the operating range are not measured. A half-hour relaxation period follows to reduce overpotentials and enable a mostly reproducible impedance measurement. The results indicate that an increase in relaxation time enhances reproducibility. Consequently, the relaxation period for the MoliP42 A is extended to three hours. When collecting the data with direct current superimposition (DC offset), it is ensured that the charge throughput does not change by more than 1 % of the nominal capacity during the measurement of one impedance spectrum. This approach minimizes the impact of non-stationarity, as otherwise the assumption of a linear and time-invariant measurement cannot be upheld.

Table 5
Scope of measurement.

	Molicel INR-21700-P42A	Samsung SDI INR-21700-50E
SoH:	100 %	100, 80 %
SoC:	10–90 % (20% steps)	10–80 % (10 % steps)
Temp.:	0–55 °C (5 °C steps)	−10, 0, 15, 25, 35, 45 °C
DC-offset:		Charge: 0.1, 0.3 C Discharge: 0.1, 0.3 C

The MoliP42 A measurement series is utilized to represent cell variations more accurately, using five cells. Additionally, it analyzes temperatures up to 55 °C with an increased number of measurement points (refer to Table 5). The test procedure is illustrated in Fig. B.1a in the appendix. Each state of charge is established through constant current charging and Coulomb counting. This process is performed in the discharge direction after reaching the last SoC (90 %).

4. Results and discussion

4.1. Sensitivity analysis

To examine the behavior of the utility index, a sensitivity analysis is conducted using a first-order polynomial with normally distributed data points as the basis. Fig. 3(a) shows the probability distribution function of two sample points around their mean value. In addition, twice the standard deviation is highlighted in each case.

To investigate the influence of the standard deviation at a constant distance between the means $\Delta\bar{x}_K = |\bar{x}_{K+} - \bar{x}_K|$, the variance is changed. Due to the calculation method described in Section 2.2, this results in different values for the utility index. In Fig. 3(a), the variance is chosen so that twice the standard deviation corresponds to half the change in the mean ($0.5 \cdot (\bar{x}_{K+} - \bar{x}_K) \approx 2\sigma$). It can be concluded that 95.4 % of the data can be clearly assigned to the respective mean. The resulting $i_{\mathrm{UI},2\sigma}$ value can also be used to estimate the possible accuracy. Fig. 3(b) shows a value of 0.5 for the aforementioned case. A threshold of 2σ was used to evaluate the index. It can be changed to adjust the sensitivity of the utility index ($i_{\mathrm{UI},1\sigma}$, $i_{\mathrm{UI},2\sigma}$, ...). If the analysis is based on the 1σ range, the resulting index is 0.75. If the standard deviation exceeds the mean change, the UI is 0, as described in Section 2.2.

The UI can be compared using the Pearson correlation coefficient, as shown in Fig. 3. This method is often used to select features for machine learning algorithms. However, it only evaluates the linear correlation of a data set, whereas the UI takes the sensitivity into account. For non-linear behavior, the sensitivity of the Pearson coefficient decreases with increasing slope. This is why alternative algorithms, such as Spearman's rank correlation, are partly being used. Ouyang et al. apply the Pearson correlation coefficient to perform a feature selection on EIS data [6]. The results in Fig. 3(b) indicate that the algorithm is not very sensitive to linear correlation and different data distributions.

The Pearson coefficient varies between 0.94 and 0.98, as shown by the comparison with the $\mathrm{UI}_{1\sigma}$ and $\mathrm{UI}_{2\sigma}$ values at $UI = 0.5$. The calculation of the utility index is therefore better suited for selecting individual features because it relates the distribution of a data set to its sensitivity.

4.2. Comparison of features from different cells

The utility index is applied to the measurement series described in Section 3.2 to evaluate the sensitivity of the individual features to temperature changes. To enhance interpretability, Appendix C includes illustrations of the raw data in the Nyquist and Bode diagrams. First, the two measurement series are compared on the basis of an identical temperature window. The classification is based on the respective SoC and temperature, as described in Section 2.2. Other states that enable further classification such as SoH and DC offset are not taken into account initially. The 2σ criterion and a temperature resolution of $\Delta T = 2$ K are used to calculate the index. Fig. 4 illustrates the results of the analysis. For this purpose, the raw data features of both measurement series, see Section 2.1.1, are compared at a reduced number of frequencies.

Fig. 4 illustrates areas with varying index values, which also differ in terms of their respective features. A strong similarity can be observed between the real part (Re-UI) and the magnitude (Mag-UI), as well as between the imaginary part (Im-UI) and the phase (Ph-UI). In the low to medium frequency range ($10^{-1} - 10^{1}$ Hz), both series of measurements show a high index for the magnitude and real part, with values well above 0.6 and a maximum value of 0.75 for the MoliP42 A. Due to the selected sensitivity criterion of 2σ, a clear assignment in the 2 K range can be achieved for 95.4 % of the data with indices > 0.5. If the UI is greater than 0.75, this applies to 99.7 % of the data. It is important to note that this is a distribution of UI values that on average lead to the described index, see Section 2.2. The sensitivity of magnitude and real part decreases with increasing frequency, while that of the

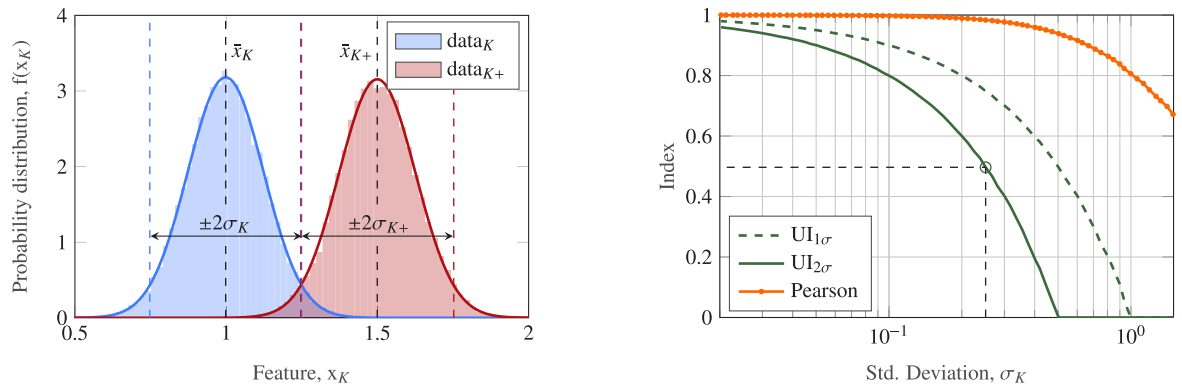

Fig. 3. Sensitivity analysis based on a first-order polynomial with a change in the normal distribution of all data groups x_K (a) Probability distribution function of two data sets around their mean value. The illustration shows the case in which: $0.5 \cdot (\bar{x}_{K+} - \bar{x}_K) \approx 2\sigma$ (b) Presentation of the results from the sensitivity analysis for the utility index compared with the Pearson correlation coefficient.

phase and imaginary part increases. The maximum is found in the imaginary part at around 50 Hz. At high frequencies, feature sensitivity decreases significantly, particularly for the MoliP42 A. This is due to the decreasing temperature sensitivity at higher frequencies. The SDI50E measurement series data remain stable up to approximately 1000 Hz due to the low influence of inductances. This is also evident from the raw data in the appendix, see Figs. C.5, C.6.

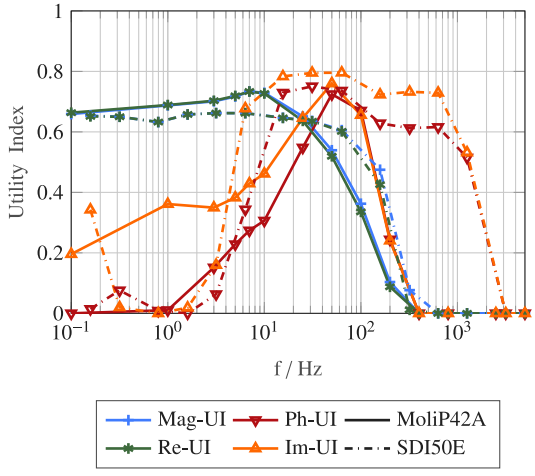

Fig. 4. UI evaluation based on raw data features. The figure illustrates the results for the SDI50E and MoliP42 A measurement series at SoH = 100 %, DC = 0 A in the temperature range 15 to 35 °C.

Table 6 can be generated by applying the evaluation algorithm to all of the described features. The table compares the ten strongest features of both measurement series.

Table 6
UI evaluation of all features from the respective measurement series. The table shows the 10 most relevant features sorted in descending order for the temperature range 15–35 °C, SoH = 100 %, DC = 0 A.

MoliP42A		SDI50E	
UI	Feature	UI	Feature
0.85	$\bar{d}_{\text{mag}}$	0.80	Im(Z(63 Hz))
0.76	Im(Z_{locMax})	0.80	Im(Z(31 Hz))
0.75	Im(Z(50 Hz))	0.78	Im(Z(16 Hz))
0.73	$\tilde{x}_{0.75,\ \text{mag}}$	0.75	$d_{\text{IR-locMin,\ real}}$
0.73	$\lvert Z(7\text{ Hz})\rvert$	0.75	arg(Z(31 Hz))
0.73	Re(Z(7 Hz))	0.74	arg(Z(63 Hz))
0.73	$\lvert Z(10\text{ Hz})\rvert$	0.73	Im(Z(320 Hz))
0.72	Re(Z(10 Hz))	0.73	arg(Z(16 Hz))
0.72	arg(Z(50 Hz))	0.73	Im(Z(631 Hz))
0.72	Re(Z(5 Hz))	0.72	$\tilde{d}$

A comparison reveals significant differences between the SDI50E and MoliP42 A measurement series. Specifically, the SDI50E series is dominated by the imaginary part and phase at medium frequencies, while the MoliP42 A features are concentrated on the magnitude and real part in the medium to low frequency range. It is therefore recommended to perform a cell-specific UI analysis. Fig. 4 illustrates these differences. The imaginary part around 50 Hz appears in both measurements. In addition, features from the statistical approach can also be found. This primarily relates to the magnitude of the MoliP42 A measurement series ($\bar{d}_{\text{mag}}$, $\tilde{x}_{0.75,\ \text{mag}}$). The $\tilde{d}$, represented in the SDI50E data, is similar to the $\bar{d}_{\text{mag}}$. However, while the $\bar{d}_{\text{mag}}$ only analyzes magnitude values, the $\tilde{d}$ represents the pairwise distance of the complex impedance in the Cartesian coordinate system. Table 6 shows that both datasets can be expected to have a high level of accuracy within the selected temperature range. The indices fall within the range of 0.75, indicating a 99.7 % probability for ΔT = 2 K. The resolution can be halved at the expense of reliability, but this still allows for distinguishability within the 2σ range.

4.3. Features in different temperature ranges

This section will discuss the suitability of features in different temperature ranges. In literature, certain characteristics are often used across the entire range, but sensitivities decrease significantly at high temperatures. The aim is to analyze which features are more suitable for this purpose and maintain a high UI with increasing temperatures. Using the MoliP42 A data and the UI evaluation method, four areas (0–15 °C, 15–30 °C, 30–45 °C, 45–55 °C) are analyzed. The effects of ageing and non-stationarity are not taken into account. The following index values show the quality of the features even when the state of charge varies, assuming knowledge of the exact SoC, cf. Section 2.2. Fig. 5 illustrates the raw data characteristics over frequency.

It is evident that the possibility of obtaining a reproducible and precise estimate decreases significantly with increasing temperature. A distinguishability of 2 K can be achieved for about 99.7 % of the data up to 30 °C. As the temperature increases, there is a clear reduction in the UI. Since the values are in the range of 0.3, it can be assumed that the 2 K temperature resolution applies to slightly more than 68 % of the data. The subsequent temperature window (45–55 °C) only has UI values of 0 and was therefore not included in the figure above. This means that the defined accuracy of 2 K cannot be achieved for high temperatures based on the MoliP42 A data. Even when analyzing the total number of features, no deviating indices can be identified in this area. As a result, this column was also removed from Table 7, which lists the strongest characteristics in descending order, taking into account the specified temperature ranges. The recorded data was taken after charging. To ensure comparability with the discharge direction, an

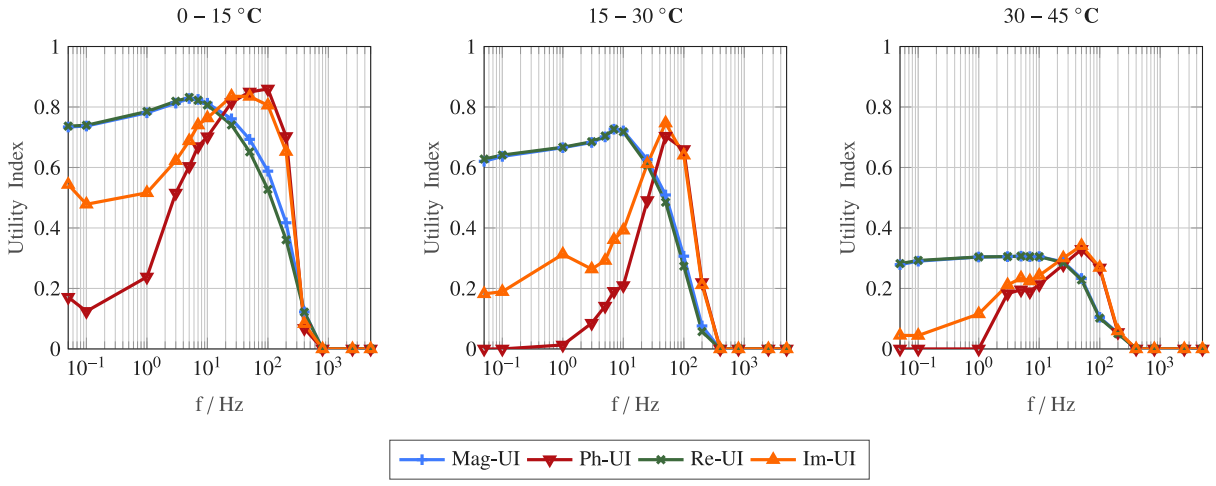

Fig. 5. Visualization of the utility indices of real and imaginary part, magnitude and phase from the data of the MoliP42 A measurement series. Subdivision based on different temperature ranges. UI evaluation with 2σ sensitivity range and $\Delta T = 2$ K.

additional table has been included in the appendix, see Table E.1. The comparison shows very similar results to those in Table 7, with only a few exceptions.

Table 7
UI rating of all features from MoliP42A. It shows the 10 most relevant characteristics sorted in descending order within a temperature range.

0–15 °C		15–30 °C		30–45 °C	
UI	Feature	UI	Feature	UI	Feature
0.86	arg(Z(100 Hz))	0.84	$\bar{d}_{\mathrm{mag}}$	0.40	$\bar{d}_{\mathrm{mag}}$
0.85	arg(Z(50 Hz))	0.76	Im(Z_{locMax})	0.36	$\tilde{x}_{0.75,\ \mathrm{mag}}$
0.84	Im(Z(25 Hz))	0.75	Im(Z(50 Hz))	0.34	Im(Z(50 Hz))
0.83	Im(Z(50 Hz))	0.73	$\lvert Z$(7 Hz)$\rvert$	0.33	Im(Z_{locMax})
0.83	Re(Z(5 Hz))	0.73	Re(Z(7 Hz))	0.31	arg(Z(50 Hz))
0.83	$\lvert Z$(5 Hz)$\rvert$	0.72	$\tilde{x}_{0.75,\ \mathrm{mag}}$	0.31	$d_{\mathrm{Max,\ real}}$
0.82	Im(Z_{locMax})	0.72	$\lvert Z$(10 Hz)$\rvert$	0.31	$R_{\mathrm{d,\ real}}$
0.82	$\lvert Z$(7 Hz)$\rvert$	0.72	Re(Z(10 Hz))	0.31	$\bar{d}_{\mathrm{mag}}$
0.82	Re(Z(7 Hz))	0.70	Re(Z(5 Hz))	0.31	Re(Z(5 Hz))
0.81	Re(Z(3 Hz))	0.70	arg(Z(50 Hz))	0.31	$\lvert Z$(5 Hz)$\rvert$

Table 7 indicates that the features remain mostly stable across different temperature ranges. For instance, all columns represent the phase and imaginary part at 50 Hz, as well as the real part at 5 Hz. However, the number of statistical features increases with rising temperature. The results demonstrate that above 15 °C the mean pairwise distance of the magnitude $\bar{d}_{\mathrm{mag}}$ is the most sensitive. Regarding the geometric characteristics, the imaginary part of the local maximum Im(Z_{locMax}) appears to be a promising option. The table demonstrates that good results can also be obtained with individual frequencies, e.g. Im(Z(50 Hz)). As Fig. 5 illustrates, sensitivity decreases notably with rising temperatures. The analysis of the SDI cells suggests a need to adapt the feature selection in the low temperature range, cf. E.4. However, confirmation of this must be obtained using a larger amount of data. The ECM features are not included in the listings due to their low index values ($i_{\mathrm{UI}} < 0.4$), which renders them unsuitable for temperature determination.

4.4. Impact of aging, SoC and non-stationarity

The suitability of the features under varying conditions is analyzed based on their state-dependent utility index. For this purpose, SoH, SoC as well as the direct current superimposition are varied. The 2σ range with a temperature resolution of $\Delta T = 2$ K is selected for evaluation. The data obtained from the SDI measurement series is utilized.

First, the characteristics are compared at $SoH_{\mathrm{C}} = 100$ % and 80 %. For this purpose, the cells were cycled until they reached 80 % of their nominal capacity. Afterwards, the EIS measurement procedure was carried out, see Section 3.2. The results are attached to the appendix (Figs. C.13–C.16). Fig. 6 illustrates the utility index at begin of life in comparison to $SoH_{\mathrm{C}} = 80$ %. The mean temperature window is used, analogous to Section 4.2.

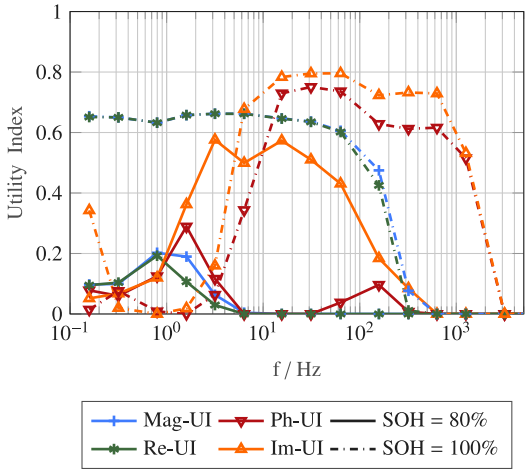

Fig. 6. Impact of aging on raw data features. Comparison between $SoH_{\mathrm{C}} = 100$ % and 80 %. Analysis based on the SDI50E measurement series between 15–35 °C, as well as the 2σ sensitivity range and $\Delta T = 2$ K.

The results indicate that sensitivity, particularly of the magnitude and real part, decreases with age due to cell-to-cell variations. These variations may be caused by mechanical stresses resulting from de-/intercalation of lithium. However, the imaginary part is proportionally less affected. Therefore, it is still possible to achieve an estimate of 2 K for the 2σ sensitivity range with features at low to medium frequencies. Compared to the results at $SoH_{\mathrm{C}} = 100$ %, a shift towards lower frequencies is observed. This suggests a change in the time constants, which is also reflected in the variation of the charge transfer semicircles, see Figs. C.7, C.15. It is therefore recommended to adjust the features over the lifetime.

Next, we will discuss the influence of a change in the state of charge and the DC superimposition. The SDI50E data is classified in such a way that there is a variation in SoC within group K, see Section 2.2. This variation affects the distribution and consequently the utility index. A SoC range of 20 % is used due to the available dataset. The comparison to the data with known SoC is illustrated in Fig. 7(a).

It is evident that a variation in the state of charge results in different impacts on the characteristics. Specifically, the imaginary part in the

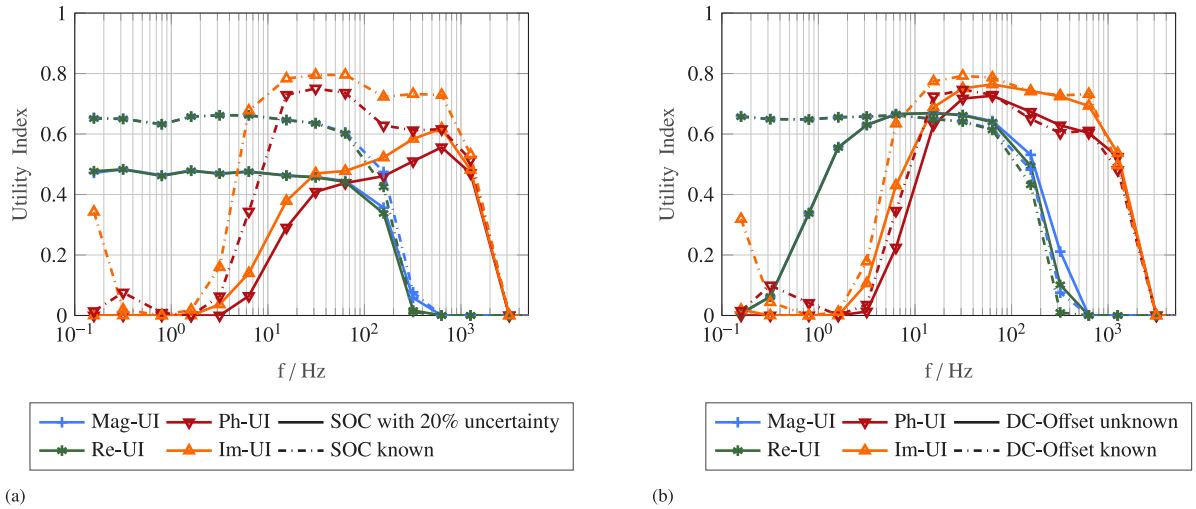

Fig. 7. Influence of varying cell states on feature sensitivity. The illustration is based on the SDI50E measurement series at SoH_C = 100 % in the temperature range 15–35 °C. The calculation is performed with a sensitivity window of 2σ and for ΔT = 2 K. (a) Impact of inaccurate SoC estimation on the characteristics. The comparison is based on the assumption of an absolute SoC accuracy of ±10 %, compared to the knowledge of the exact state of charge. (b) Influence of a constant current superimposition.

medium frequency range is significantly affected, while the influence diminishes at high frequencies. Therefore, it can be inferred that higher frequencies are more suitable for temperature determination measurements with inaccurate SoC estimation. This conclusion is supported by other research groups, cf. [12,13]. Based on the provided data, the imaginary part at 631 Hz represents the optimum. A significant reduction in the UI can be observed over the entire frequency range when compared to the data with precise SoC estimation. This is also evident in Table E.2, which shows a shift of the features to higher frequencies, with an increasing representation from the statistical set. In general, it can be stated that the characteristics of the raw data predominate.

For online impedance measurements, it is important to consider not only changes in the state of charge but also the effects of non-stationarity. To achieve this, an evaluation of the remaining sensitivity during direct current superimposition is performed using the raw data characteristics. As explained in Section 3, we examine C-rates up to 0.3 C in both charging and discharging directions. Fig. 7(b) depicts the results of the UI analysis. The calculation of the index value changes due to a different classification, see Section 2.2. For the data with known DC offset, all C-rates are evaluated individually, while for "DC offset unknown" they are combined into a group.

Fig. 7(b) shows a slight influence for mid to high frequencies. In contrast, the low frequency values, especially the real part and magnitude, are significantly reduced. When comparing the "DC-Offset known" data with the results without considering the C-rate, see Fig. 4, there are barely any differences. This shows that the individual direct current superimpositions can be easily distinguished, as can be seen in Fig. C.11. From this observation it can be concluded that there is a potential to correct the effects as recommended in the literature, cf. [11]. However, for the data presented, good results can be obtained in the intermediate temperature range even without compensation or knowledge of the effects. Table E.3 in the appendix shows a high potential for the imaginary part at medium frequencies. With an index of 0.76, it can be assumed that the 2 K temperature resolution can be achieved on 99.7 % of the data despite the DC current.

In order to facilitate a comparison between the UI results and a method that is commonly employed in literature, selected impedance features are approximated using the extended Arrhenius equation:

$$Z(T) = A \cdot \exp\left(\frac{-E_a}{R_c \cdot T}\right) + B. \tag{12}$$

The analysis is based on an SoC accuracy of ±10 % and an unknown constant current superimposition at SoH_C = 100 %. To account for ageing, the same analysis is also carried out for SoH_C = 80 %. The results can be seen in Fig. 8.

Fig. 8 shows that two different features are used for the evaluation (Im(Z(631 Hz)), Im(Z(31 Hz))). The feature selection is based on the utility index, cf. Table E.5. To ensure comparability with the UI method, the temperature error is calculated using twice the standard deviation. At SoH_C = 100 % and temperatures between 15–35 °C, the error is 1.48 K. The associated utility index has a value of 0.58. Utilizing equation (8) and the assumptions delineated in Section 4.1, the temperature error can be calculated from the utility index with

$$T_{res} = \frac{2\ \mathrm{K} \cdot (1 - i_{UI})}{0.5}. \tag{13}$$

In this instance, the change in the mean values $|\Delta x|$ is substituted with the temperature resolution T_{res}. For i_{UI} = 0.58, this yields a value of 1.68 K. The discrepancy can be attributed to the disparate methodologies employed. Nevertheless, both approaches yield comparable results. This can also be confirmed by the data at SoH_C = 80 %, which shows a value of 2.37 K and a UI of 0.37, resulting in T_{res} = 2.52 K.

4.5. Discussion

The reduction of dependencies and sensitivities to a single index leads to limitations that must be taken into account when interpreting and selecting features. It is worth noting that the achievable accuracies are based on an average of all calculated UI values for the corresponding groups. Depending on the classification, lower or higher values may occur. Additionally, the utility index assumes normally distributed dependencies, which may deviate from reality. Furthermore, the algorithm only provides sensitivity information and does not allow for conclusions about trends. It may be possible to combine this with correlation coefficients. To obtain meaningful results, at least three cells and a sufficient number of different cell states are required. However, it should be noted that the utility index may change as the number of cells and cell states increase due to a more accurate representation of the probability. When measuring the SDI cells, low superimposed currents were used, which may have a minor impact. It can be reasonably anticipated that a notable impact will be observed as the current increases, particularly with regard to impedance features at low frequencies. Therefore, it is necessary to confirm the influence of non-stationarity at higher current rates and other profiles. Furthermore, the present manuscript exclusively utilizes laboratory data. However, the method can also be applied to noisy data, as is expected in the vehicle environment. This may result in a deviation from the features recommended in this manuscript.

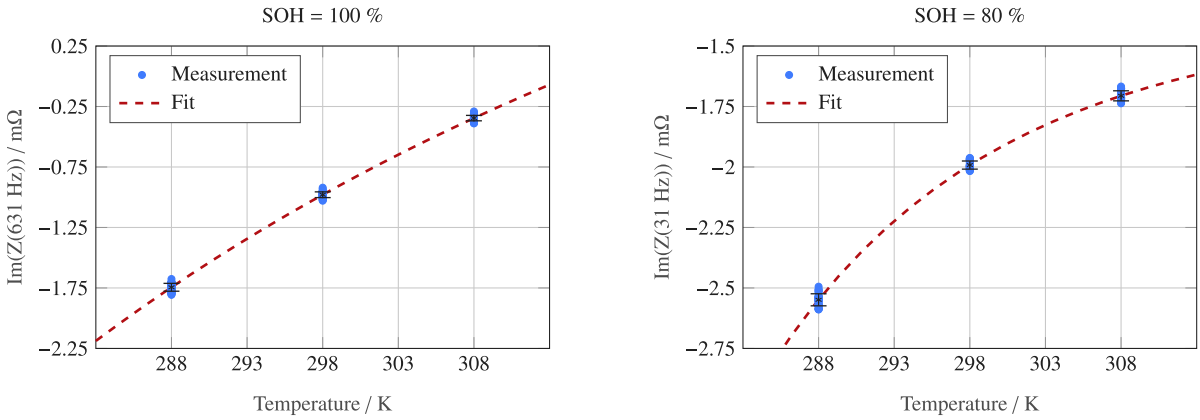

(a) (b)

Fig. 8. Temperature determination based on UI feature recommendation. The figure shows the individual characteristics as well as their standard deviation and the approximation using the extended Arrhenius equation for SoC = 50 % and between 15 and 35 degrees. It is based on an absolute SoC accuracy of ±10 % and an unknown constant current superimposition. The results for SoH_C = 100 % are shown in (a), those for SoH_C = 80 % in (b).

5. Conclusion

Electrochemical impedance spectroscopy measurements can be influenced by varying cell states, particularly during online applications. Additionally, inductive effects may occur from measuring devices or the surrounding environment. Due to these multidimensional dependencies, it is difficult to recommend a generally valid feature for temperature estimation. Rather, it is advisable to choose a cell-specific approach.

The sensitivity analysis were conducted and the utility index was calculated to evaluate characteristics from the impedance spectrum, while also considering the influence of changing cell states. The calculated index provides information about the maximum achievable accuracy for temperature determination. Four different approaches were used to extract 143 features from the impedance spectrum. It turns out that the characteristics resulting from an equivalent electrical circuit approximation do not have a significant potential for temperature determination. Their indices were clearly below 0.4, which is why the ECM features are not among the top 10 with the highest UI in any of the various conditions. From the list of geometric features, the imaginary part of the local maximum ($\mathrm{Im}(Z_{\mathrm{locMax}})$) has been shown to be appropriate, cf. Table 6, 7, E.2, E.3. Additionally, the lists of key characteristics contain some of the statistical approaches. The mean pairwise distance is particularly promising. In general, the features extracted from raw data, particularly the imaginary part and phase, perform well in all investigations. Based on these, a temperature estimate in the range of 2 K is still possible for around 95.4 % of the data between 15–35 °C, even at SoH_C = 80 %. This was also investigated using the Arrhenius equation, taking into account additional effects such as SoC uncertainty and the superposition of direct currents. These results confirm the suitability of the presented UI-based method.

With increasing age, a shift to lower frequencies was observed. For online operation, it is advisable to adjust the characteristics over the lifetime. The opposite behavior occurs when the state of charge or the superimposed current changes. Therefore, for applications under load or with inaccurate SoC estimation, the use of higher frequencies is preferable. The behavior in different temperature ranges was also analyzed. The MoliP42 A cells did not exhibit any sensitivity above 45 °C within the 2σ range. Below this temperature, the sensitivity was very good, particularly for the raw data features, as well as for those from the statistics and geometry. The index decreases as the temperature increases. It was not demonstrated that adapting the feature selection at different temperature ranges leads to a significant improvement. The analysis of the SDI cells indicates that an adjustment of the features at lower temperatures may be necessary. However, this conclusion needs to be verified against a larger database.

This article highlights the potential of the utility index and its applicability to impedance spectra of lithium-ion batteries. The demonstration was carried out through two independent series of measurements on different cells and under various conditions. The usability of the utility index for machine learning algorithms as well as under dynamic load conditions represents a future field of research.

CRediT authorship contribution statement

Tobias Hackmann: Writing – review & editing, Writing – original draft, Visualization, Validation, Software, Methodology, Investigation, Formal analysis, Data curation, Conceptualization. **Sebastian Esser:** Writing – review & editing, Software, Methodology. **Michael A. Danzer:** Writing – review & editing, Supervision.

Declaration of competing interest

The authors declare the following financial interests/personal relationships which may be considered as potential competing interests: Tobias Hackmann reports financial support was provided by BMW Group. Tobias Hackmann reports a relationship with BMW Group that includes: employment. If there are other authors, they declare that they have no known competing financial interests or personal relationships that could have appeared to influence the work reported in this paper.

Data availability

The authors do not have permission to share data.

Declaration of Generative AI and AI-assisted technologies in the writing process

During the preparation of this work the author(s) used DeepL in order to improve language. After using this tool/service, the author(s) reviewed and edited the content as needed and take(s) full responsibility for the content of the publication.

Acknowledgments

The authors would like to thank Dr. Jose Lopez de Arroyabe (BMW Group), Doan Phi Dang (BMW Group), Professor Oliver Bohlen (University of Applied Sciences Munich) and Christian Rosenmüller (University of Applied Sciences Munich) for providing and performing the measurement series.

Funding

This work was supported by the BMW Group, Munich, Germany.

Appendix A. Literature review on temperature estimation

Table A.1
Literature review on temperature estimation using EIS.

Ref.	Temperature	Method	Feature	Further dependencies			Accuracy	Chemistry
	Range			SOH	SOC	DC-Offset		
[18]	−60–20 °C	EIS + ECM	R_{ct}	–	–	–	–	Ni-based | C
[3]	−20–66 °C	EIS + ECM + Arrh. EIS + LUT	arg(Z(40 Hz)), R_s, R_{SEI}	–	5 %–95 %	–	–	LCO | C LFP | C –
[42]	−10–50 °C	EIS + LUT	arg(Z(40 Hz))	–	5 %–95 %	–	–	LCO | C
[28]	0–25 °C	EIS + mod. Arrh.	Re(Z(10.3 kHz))	–	50 %	–	max. Error = 0.17 K (SOC known) max. Error = 2.5 K (SOC unknown)	LCO+NCA | C
[17]	−13–55 °C	EIS + ECM + Arrh. EIS + LUT	R_{ct}	–	–	–	–	–
[2]	−20–50 °C	EIS + mod. Arrh.	f(Im = 0)	600 cyc.	20 %– 100 %	–	–	LFP | C NCA | C
[26]	−20–45 °C	EIS + Arrh. & 2 ord. polynom	Re(Z(215 Hz)) - R_s	–	10 %–90 %	+/−10A +/−20A Drivecycle	MAE = 0.6 K (Drivecycle)	LFP | C
[43]	−20–50 °C	EIS	arg(Z(Range)), Re(Z(Range))	100 %– 75 %	10 %– 100 %	DCH: 0.5–2.5 C CH: 1 C	MAE = 1 K (Pulse profile, T = 25–28 °C) MAE = 1.5 K (Pulse profile, T = −10–(−5) °C)	–
[44]	−20–45 °C	EIS + TM + diff. KF	Re(Z(215 Hz)) - R_s	–	10 %–90 %	–	RMSE = 2.04 K (EKF + Z') RMSE = 2.49 K (KF + Tsurf) RMSE = 1.43 K (DEKF + Z') RMSE = 0.36 K (DKF + Tsurf)	LFP | C
[13]	−10–95 °C	EIS + Arrh. + 1 ord. Polynom	Im(Z(300 Hz))	–	0 %–100 %	–	MAE = 5.6 K max. Error = 11.4 K	LCO
[8]	0–45 °C	EIS	arg(Z(79.4 Hz))	100 %– 80 %	30 %–70 %	–	–	LFP
[19]	−20–50 °C	EIS + LUT & optimization	|Z(50 Hz)|, arg(Z(50 Hz)), Re(Z(50 Hz)), Im(Z(50 Hz))	–	20 %–80 %	–	Mean Std. = 0.7 K RMSE = 0.4 K	LFP
[45]	−10–40 °C	EIS + 2 ord. polynom	arg(Z(1 kHz))	–	0 %–100 %	–	max. Error = 3.16 K (SOC known) max. Error = 4.11 K (SOC unknown)	LTO
[46]	−20–50 °C	EIS	f(Im = 0) f(Im ≠ 0)	–	20 %– 100 %	–	–	LFP
[20]	−20–50 °C	EIS + LUT & optimization	|Z(50 Hz)|, arg(Z(50 Hz)), Re(Z(50 Hz)), Im(Z(50 Hz))	–	20–80 %	–	MSE = 0.5 K (SOC known) MSE = 0.7 K (SOC unknown)	LFP
[27]	10–25 °C	EIS + 2D-TM + KF/EKF	Re(Z(215 Hz)) - R_s	–		–	RMSE = 0.2–0.7 K	LFP | C
[25]	5–55 °C	EiS + 2 ord. polynom	f(Im = 0)	–	29, 100 %	–	–	NCA

(*continued on next page*)

Table A.1 (*continued*).

Ref.	Temperature	Method	Feature	Further dependencies			Accuracy	Chemistry
	Range			SOH	SOC	DC-Offset		
[47]	10–30 °C	EIS + TM + mod. Arrh.	$\lvert Z(500\ \text{Hz})\rvert$	–	–	–	–	
[48]	−20–40 °C	EIS + relax. model	arg(Z(10 Hz))	–	0 %–100 %	Puls: −1.5–1.5 C	max. Error = 2 K (T = 10–15 °C) max. Error = 3 K (T = 20–25 °C)	LFP | C
[23]	−40–0 °C	EIS + 3 ord. polynom	Re(Z(8 Hz))	–	50, 80 %	–	–	NCA | C
[4]	10-TR	EIS	arg(Z(40 Hz))	–	–	–	–	NMC
[49]	−20–50 °C	EIS + LUT & optimization	Re(Z(133 Hz)), Im(Z(133 Hz)) Re(Z(630 Hz)), Im(Z(630 Hz))	–	20 %–80 %	−1–0.5 C	avg. MSE = 1.1 K (without crosstalk) avg. MSE = 1.1 K (with crosstalk) avg. MSE = 4 K (with (D)CH) avg. MSE = 3.8 K (with (D)CH & crosstalk comp.)	NMC
[50]	5–45 °C	EIS + exp. Func.	arg(Z(10 Hz))	–	10 %–90 %	Step: +/−20 A NEDC: −60–40 A	avg. Error = 0.33 K (T. Range = 15–25 °C, Step) avg. Error = 0.5 K (T. Range = 25–26.5 °C, NEDC)	LFP
[29]	5–55 °C	EIS + Arrh.	arg(Z(various))	93 %–59 %	0 %–100 %	–	MAE = 1 K	LFP
[24]	10–55 °C	EIS + 1 ord. Polynom	Im(Z(200 Hz))	100 %– 80 %	0 %–100 %	–	RMSE = 1.41 K	LCO
[22]	10–60 °C	EIS + ANN	Re(Z(Range))	100 %– 85 %	10 %–90 %	DCH: 0–1.5 C CH: 1 C	avg. RMSE = 1 K | max. RMSE = 5 K avg. RMSE = 0.5 K avg. RMSE = 0.7 K	- NMC NCA
[51]	5–55 °C	EIS + Arrh.	Im(Z(10 Hz))	–	10 %–90 %	–	max. Error = 1.5 K (SOC unknown, T = 25 °C)	
[6]	10–60 °C	EIS + SVR	Im(Z(263 Hz)) Im(Z(524 Hz))	–	30 %– 100 %	–	RMSE = 0.23 K (SOC known, 263 Hz) RMSE = 0.57 K (SOC unknown, 263 Hz) RMSE = 0.43 K (SOC known, 524 Hz) RMSE = 0.69 K (SOC unknown, 524 Hz)	NMC
[52]	−20-(−2) °C −20–10 °C 0–18 °C	EIS + LUT + NLLS	Re(Z(Range)), Im(Z(Range))	–	50 %	+/−25 A (AC) +/−35 A (AC) Driving Profil	abs. Error = 0.6 K abs. Error = 1.1 K abs. Error = 1 K	–
[21]	−10–60 °C	EIS + ANN	Re(Z(Range)), Im(Z(Range))	–	10 %–90 %	−0.5 C, 0.5 C	RMSE = <0.9 K	NCA

Appendix B. Measurement procedure

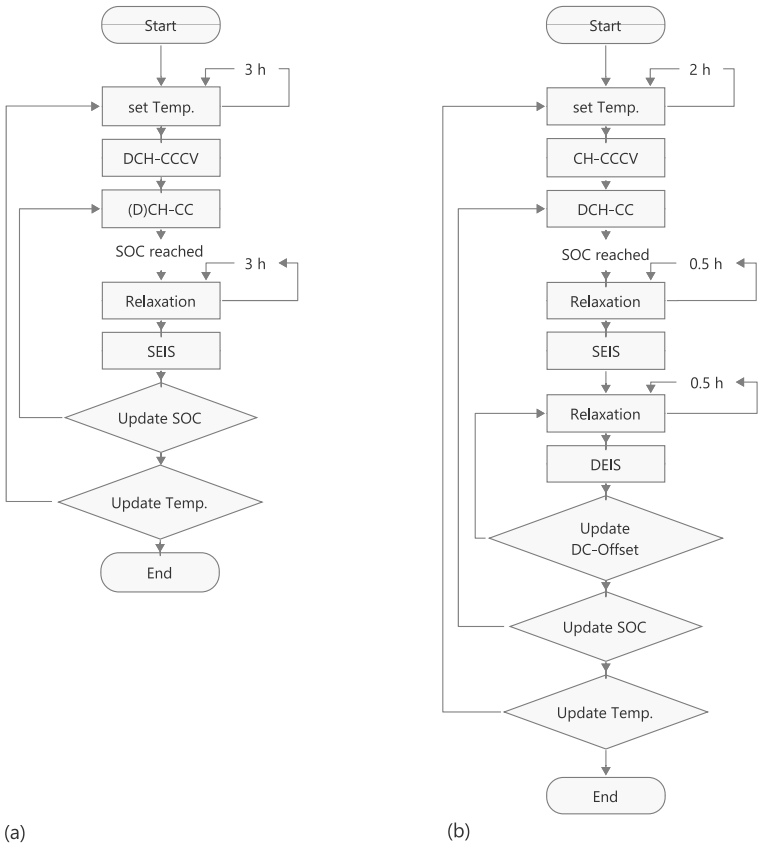

Fig. B.1. Flow chart illustrating the test procedure for both series of measurements. (a) shows the MoliP42A, (b) the SDI50E. SEIS refers to EIS measurements under stationary conditions, DEIS to those carried out during (dis)charging.

Appendix C. Raw data in Nyquist & Bode diagram

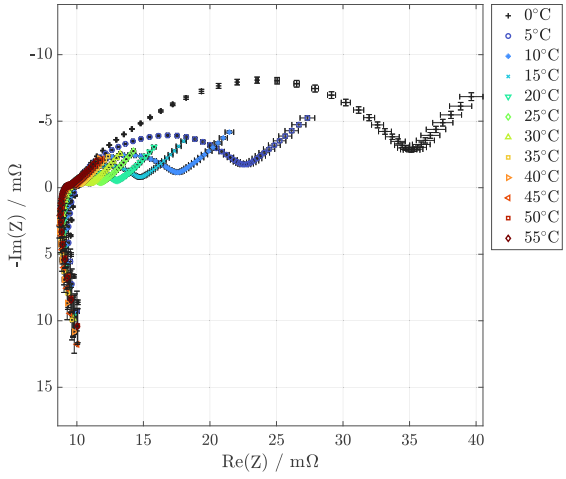

Fig. C.1. Nyquist diagram shows the effect of temperature changes based on the MoliP42 A measurement series at SoH_C = 100 %, SoC = 50 %.

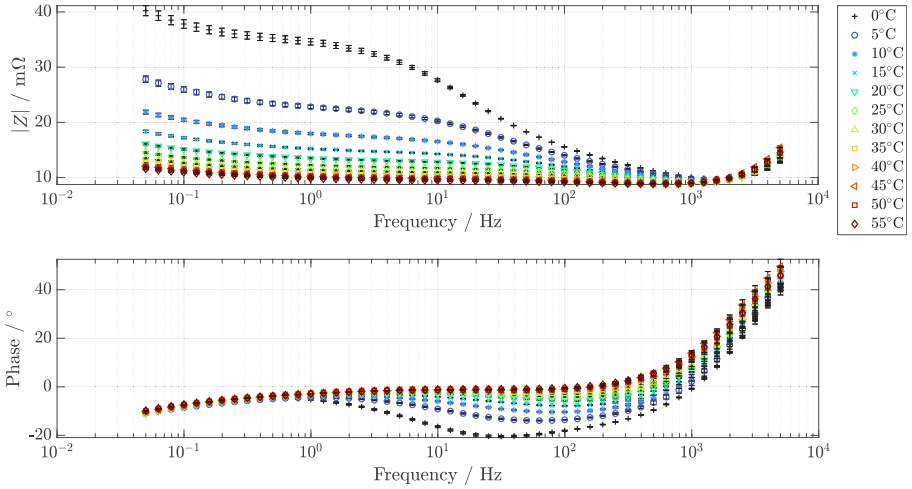

Fig. C.2. Bode diagram shows the effect of temperature changes based on the MoliP42 A measurement series at SoH_C = 100 %, SoC = 50 %.

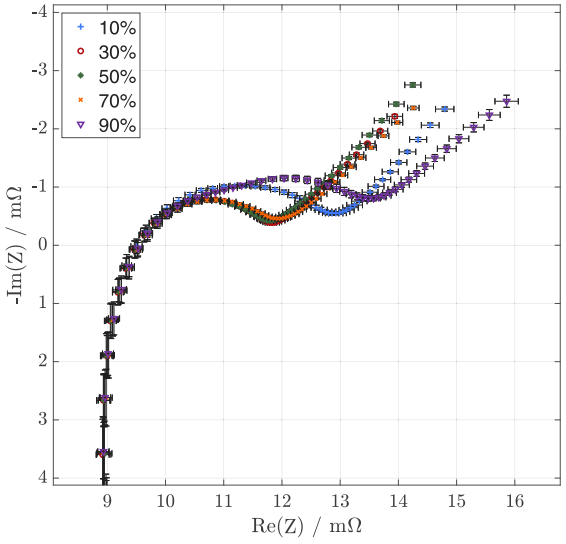

Fig. C.3. Nyquist diagram shows the effect of SoC changes based on the MoliP42 A measurement series at SoH_C = 100 %, T = 25 °C.

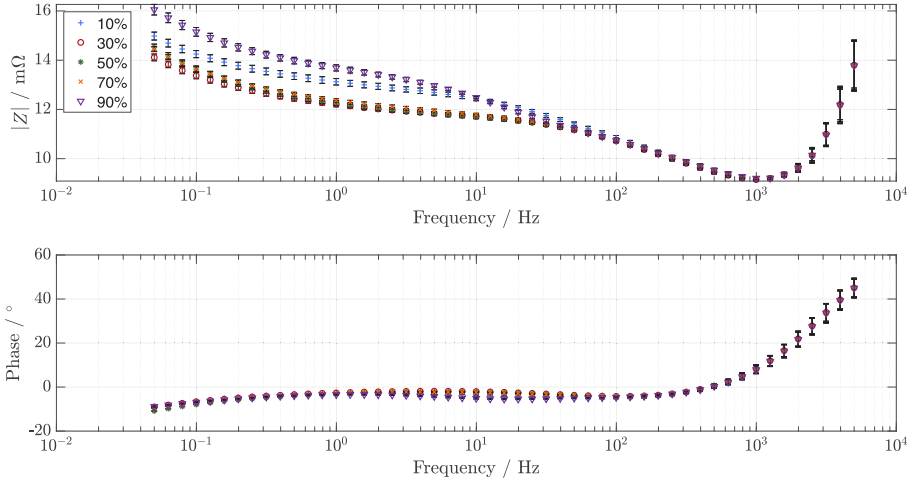

Fig. C.4. Bode diagram shows the effect of SoC changes based on the MoliP42 A measurement series at SoH_C = 100 %, T = 25 °C.

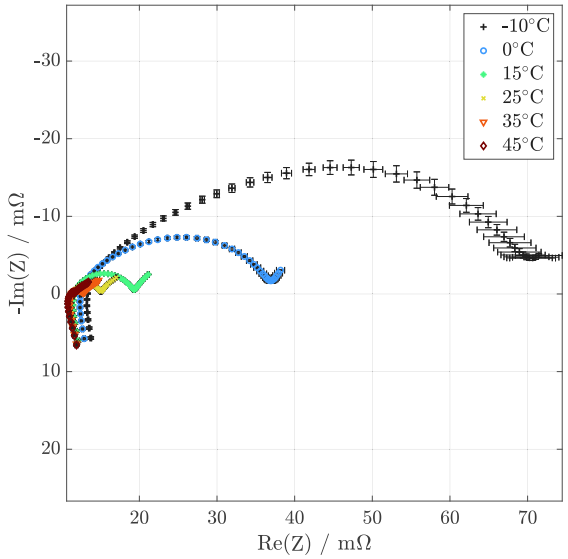

Fig. C.5. Nyquist diagram shows the effect of temperature changes based on the SDI50E measurement series at SoH_C = 100 %, SoC = 50 %.

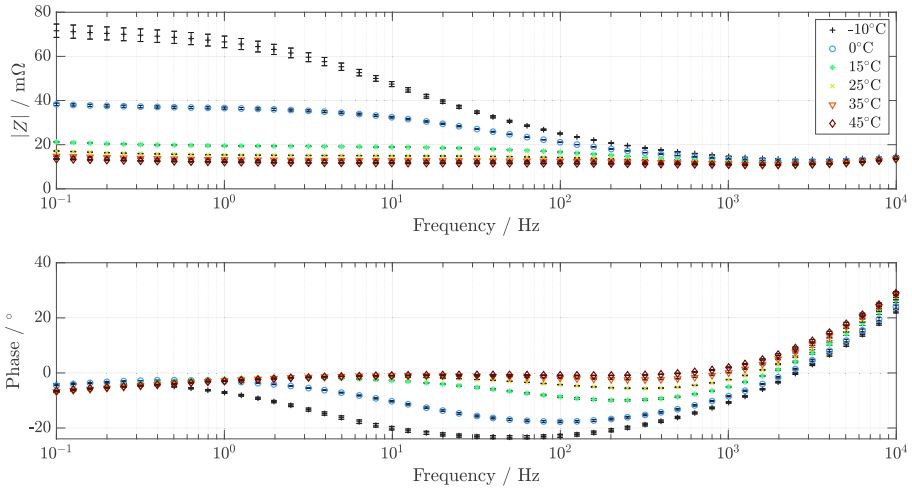

Fig. C.6. Bode diagram shows the effect of temperature changes based on the SDI50E measurement series at SoH_C = 100 %, SoC = 50 %.

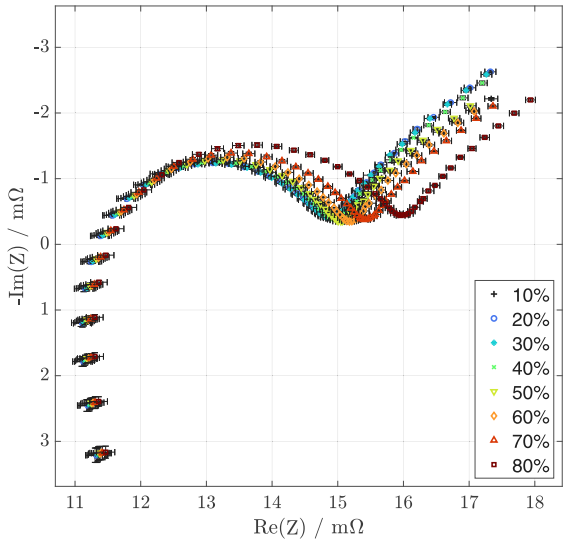

Fig. C.7. Nyquist diagram shows the effect of SoC changes based on the SDI50E measurement series at SoH_C = 100 %, T = 25 °C.

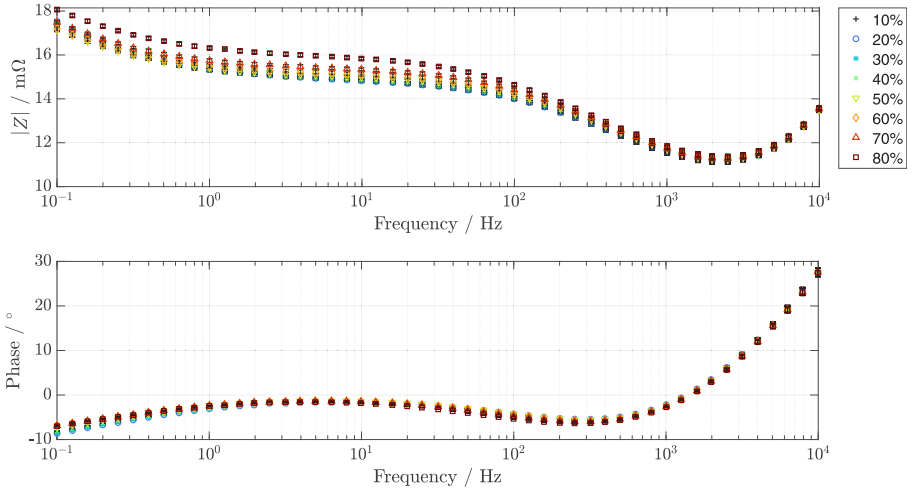

Fig. C.8. Bode diagram shows the effect of SoC changes based on the SDI50E measurement series at SoH_C = 100 %, T = 25 °C.

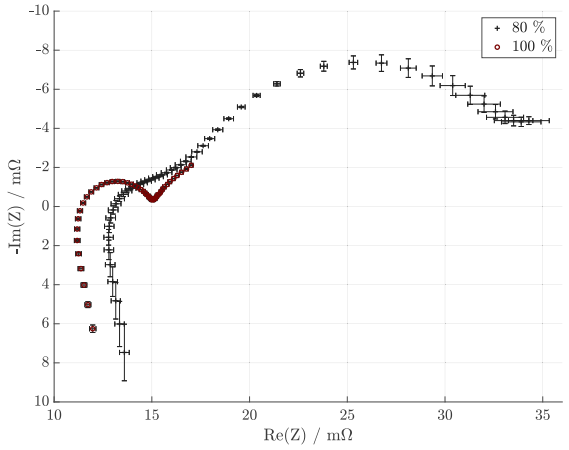

Fig. C.9. Nyquist diagram shows the effect of SoH changes based on the SDI50E measurement series at SoC = 50 %, T = 25 °C.

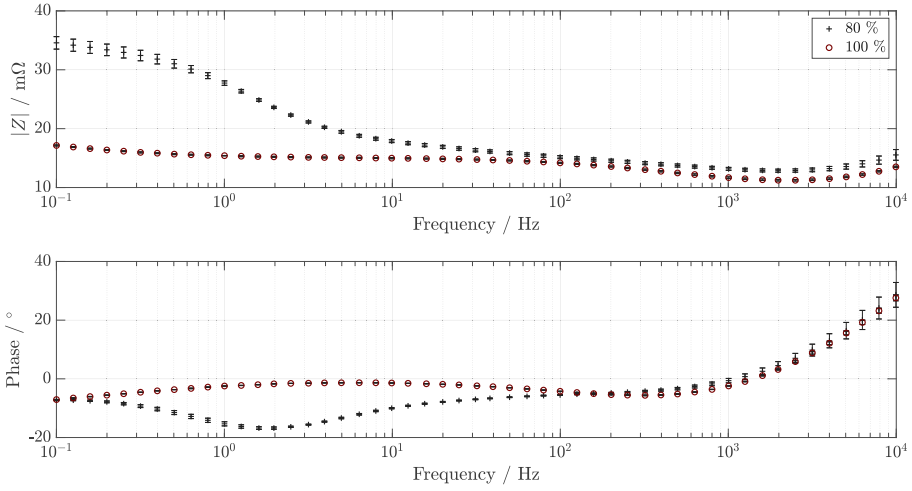

Fig. C.10. Bode diagram shows the effect of SoH changes based on the SDI50E measurement series at SoC = 50 %, T = 25 °C.

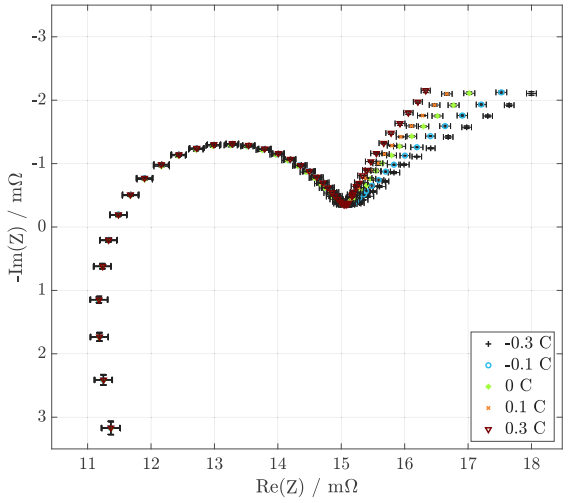

Fig. C.11. Nyquist diagram shows the effect of a superimposed constant current based on the SDI50E measurement series at SoH_C = 100 %, SoC = 50 %, T = 25 °C.

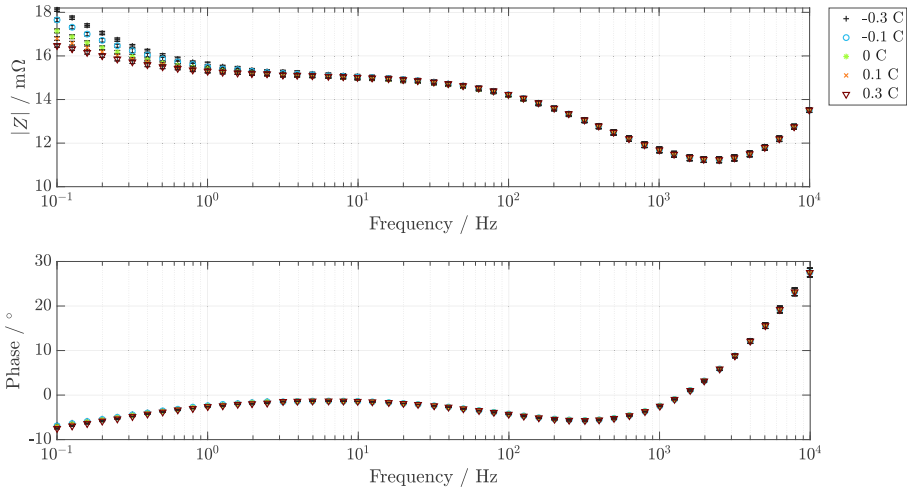

Fig. C.12. Bode diagram shows the effect of a superimposed constant current based on the SDI50E measurement series at SoH_C = 100 %, SoC = 50 %, T = 25 °C.

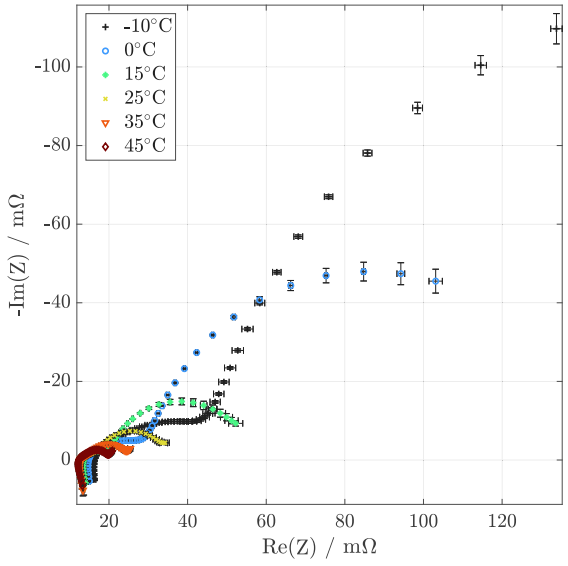

Fig. C.13. Nyquist diagram shows the effect of temperature changes based on the SDI50E measurement series at SoH_C = 80 %, SoC = 50 %.

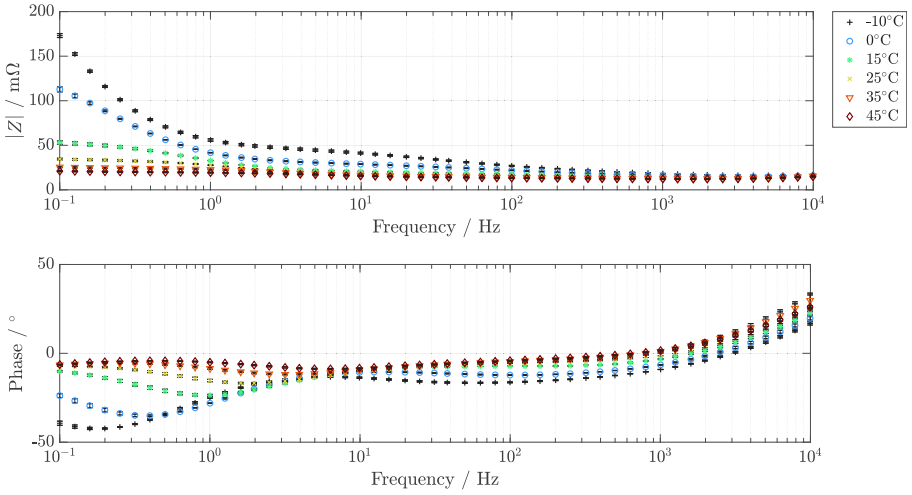

Fig. C.14. Bode diagram shows the effect of temperature changes based on the SDI50E measurement series at SoH_C = 80 %, SoC = 50 %.

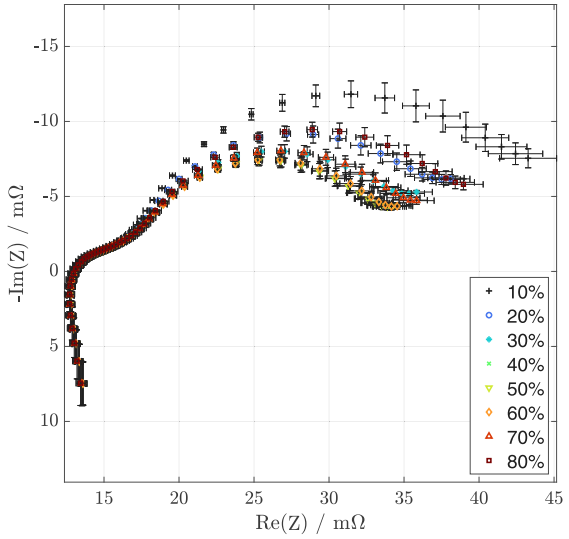

Fig. C.15. Nyquist diagram shows the effect of SoC changes based on the SDI50E measurement series at SoH_C = 80 %, T = 25 °C.

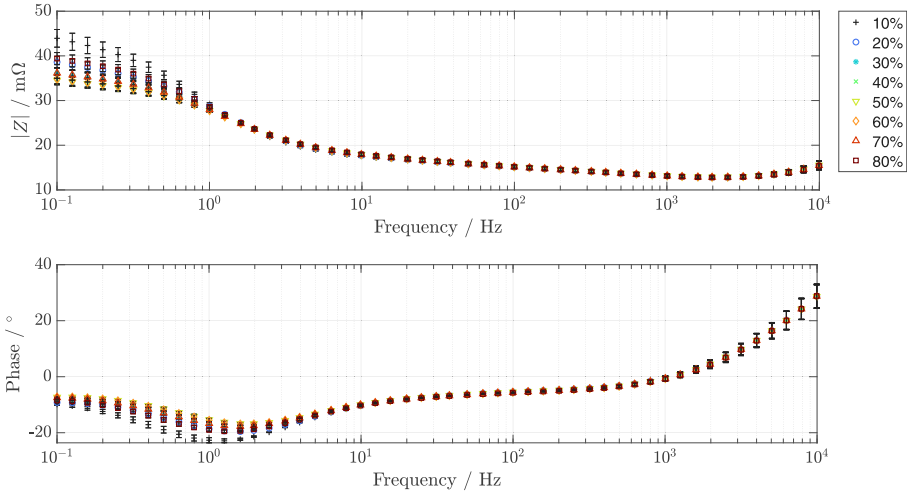

Fig. C.16. Bode diagram shows the effect of SoC changes based on the SDI50E measurement series at SoH_C = 80 %, T = 25 °C.

Appendix D. Feature description

Table D.1
List of features from ECM.

Name	Description
R_0	Ohmic resistance
L_0	Serial inductance
R_{RL}	Resistance R of RL-Element
L_{RL}	Inductance L of RL-Element
R_{RCPE1}	Resistance R of the first ZARC-Element
Q_{RCPE1}	Parameter Q_{CPE} of the first ZARC-Element
n_{RCPE1}	Factor n of the first ZARC-Element
R_{RCPE2}	Resistance R of the second ZARC-Element
Q_{RCPE2}	Parameter Q_{CPE} of the second ZARC-Element
n_{RCPE2}	Factor n of the second ZARC-Element
R_{RCPE3}	Resistance R of the third ZARC-Element
Q_{RCPE3}	Parameter Q_{CPE} of the third ZARC-Element
n_{RCPE3}	Factor n of the third ZARC-Element

Appendix E. Further UI analysis

Table E.1
UI rating of all features from MoliP42A. It shows the 10 most relevant characteristics sorted in descending order within a temperature range. The data is based on the stationary impedance measurement after discharge.

0–15 °C		15–30 °C		30–45 °C	
UI	Feature	UI	Feature	UI	Feature
0.91	arg(Z(100 Hz))	0.80	$\tilde{d}_{mag}$	0.40	$R_{d,\ real}$
0.91	Re(Z(5 Hz))	0.74	$\tilde{x}_{0.75,mag}$	0.38	$\tilde{d}_{mag}$
0.91	|Z(5 Hz)|	0.74	$\tilde{d}_{mag}$	0.36	$\tilde{x}_{0.75,mag}$
0.91	|Z(7 Hz)|	0.73	Im(Z(50 Hz))	0.33	$d_{max,\ real}$
0.90	Im(Z(50 Hz))	0.72	Re(Z_{locMin})	0.32	Im(Z(50 Hz))
0.90	Im(Z_{locMax})	0.70	arg(Z(50 Hz))	0.32	Im(Z_{locMax})
0.90	Re(Z(7 Hz))	0.70	Im(Z(25 Hz))	0.31	$\tilde{d}_{mag}$
0.90	|Z(10 Hz)|	0.70	Im(Z_{locMax})	0.31	arg(Z(50 Hz))
0.89	Re(Z(3 Hz))	0.69	arg(Z(100 Hz))	0.30	$\sigma^2_{d,\ real}$
0.89	|Z(3 Hz)|	0.68	Re(Z(5 Hz))	0.29	$\tilde{d}_{real}$

Table E.2
The table illustrates the influence of an inaccurate SoC estimate on feature selection. The calculation is based on the SDI50E measurement series in the temperature range 15–35 °C, as well as the 2σ sensitivity range and ΔT = 2 K. A SoC accuracy of ±10 % is compared with the knowledge of the exact state of charge.

SoC known		SoC with 20 % uncertainty	
UI	Feature	UI	Feature
0.80	Im(Z(63 Hz))	0.62	Im(Z(631 Hz))
0.80	Im(Z(31 Hz))	0.58	Im(Z(320 Hz))
0.78	Im(Z(16 Hz))	0.56	arg(Z(631 Hz))
0.75	$d_{IR\text{-}locMin,\ real}$	0.54	Im(Z_{locMax})
0.75	arg(Z(31 Hz))	0.52	Im(Z(158 Hz))
0.74	arg(Z(63 Hz))	0.52	$\tilde{x}_{0.25,imag}$
0.73	Im(Z(320 Hz))	0.52	$d_{IR\text{-}locMin,\ real}$
0.73	arg(Z(16 Hz))	0.51	arg(Z(320 Hz))
0.73	Im(Z(631 Hz))	0.50	$\tilde{x}_{IQR,\ real}$
0.72	$\tilde{d}$	0.50	$\tilde{d}_{real}$

Table E.3
The table shows the influence of a superimposed constant current on the feature. Results are based on the SDI50E measurement series in the temperature range 15–35 °C, as well as across all SoC's at SoH_C = 100 %.

DC-Offset known		DC-Offset unknown	
UI	Feature	UI	Feature
0.79	Im(Z(31 Hz))	0.76	Im(Z(63 Hz))
0.79	Im(Z(63 Hz))	0.75	Im(Z(31 Hz))
0.77	Im(Z(16 Hz))	0.74	Im(Z(158 Hz))
0.75	arg(Z(31 Hz))	0.73	arg(Z(63 Hz))
0.74	$d_{IR\text{-}locMin,\ real}$	0.73	Im(Z_{locMax})
0.74	$\tilde{x}_{IQR,\ real}$	0.72	Im(Z(320 Hz))
0.74	Im(Z(158 Hz))	0.72	arg(Z(31 Hz))
0.73	Im(Z(631 Hz))	0.70	$d_{IR\text{-}locMin,\ real}$
0.73	arg(Z(63 Hz))	0.69	Im(Z(631 Hz))
0.73	Im(Z(320 Hz))	0.69	Im(Z(16 Hz))

Table E.4
UI rating of all features from the SDI50E measurement series. It shows the ten most relevant features sorted in descending order within a temperature range, taking into account all SoC's for SoH_C = 100 %.

–10–15 °C		15–35 °C	
UI	Feature	UI	Feature
0.83	|Z(158 Hz)|	0.80	Im(Z(63 Hz))
0.80	Re(Z(158 Hz))	0.80	Im(Z(31 Hz))
0.73	Re(Z(63 Hz))	0.78	Im(Z(16 Hz))
0.71	|Z(320 Hz)|	0.75	$d_{IR\text{-}locMin,\ real}$
0.67	arg(Z(3 Hz))	0.75	arg(Z(31 Hz))
0.66	|Z(63 Hz)|	0.74	arg(Z(63 Hz))
0.65	$d_{IR\text{-}locMin,\ mag}$	0.73	Im(Z(320 Hz))
0.64	arg(Z(6 Hz))	0.73	arg(Z(16 Hz))
0.63	$\tilde{d}_{mag}$	0.73	Im(Z(631 Hz))
0.63	Re(Z(31 Hz))	0.72	$\tilde{d}$

Table E.5
Influence of an inaccurate SoC estimate (±10 %) and an unknown DC offset on the feature selection. The calculation is based on the SDI50E measurement series in the temperature range 15–35 °C, as well as the 2σ sensitivity range and ΔT = 2 K.

SoH_C = 100 %		SoH_C = 80 %	
UI	Feature	UI	Feature
0.58	Im(Z(631 Hz))	0.37	Im(Z(31 Hz))
0.57	Im(Z(320 Hz))	0.36	Im(Z(63 Hz))
0.53	Im(Z_{locMax})	0.31	Im(Z(16 Hz))
0.52	arg(Z(631 Hz))	0.29	Im(Z(158 Hz))
0.52	Im(Z(158 Hz))	0.22	|Z(1.6 Hz)|
0.50	arg(Z(320 Hz))	0.22	$\tilde{x}_{0.75,\ mag}$
0.48	$d_{IR\text{-}locMax,\ real}$	0.13	Im(Z(320 Hz))
0.48	$d_{IR\text{-}locMin,\ real}$	0.12	f_{locMin}
0.47	Im(Z(63 Hz))	0.12	$\tilde{x}_{IQR,\ mag}$
0.47	arg(Z(158 Hz))	0.11	arg(Z(158 Hz))

References

[1] L. Zhou, X. Lai, B. Li, Y. Yao, M. Yuan, J. Weng, Y. Zheng, State estimation models of lithium-ion batteries for battery management system: Status, challenges, and future trends, Batteries 9 (2) (2023) 131, http://dx.doi.org/10.3390/batteries9020131.

[2] L. Raijmakers, D.L. Danilov, J. van Lammeren, M. Lammers, P. Notten, Sensorless battery temperature measurements based on electrochemical impedance spectroscopy, J. Power Sources 247 (2014) 539–544, http://dx.doi.org/10.1016/j.jpowsour.2013.09.005.

[3] R. Srinivasan, B.G. Carkhuff, M.H. Butler, A.C. Baisden, Instantaneous measurement of the internal temperature in lithium-ion rechargeable cells, Electrochim. Acta 56 (17) (2011) 6198–6204, http://dx.doi.org/10.1016/j.electacta.2011.03.136.

[4] R. Srinivasan, P.A. Demirev, B.G. Carkhuff, Rapid monitoring of impedance phase shifts in lithium-ion batteries for hazard prevention, J. Power Sources 405 (2018) 30–36, http://dx.doi.org/10.1016/j.jpowsour.2018.10.014.

[5] A. La Rue, P.J. Weddle, M. Ma, C. Hendricks, R.J. Kee, T.L. Vincent, State-of-charge estimation of LiFePO 4 –Li 4 Ti 5 O 12 batteries using history-dependent complex-impedance, J. Electrochem. Soc. 166 (16) (2019) A4041–A4046, http://dx.doi.org/10.1149/2.0221916jes.

[6] K. Ouyang, Y. Fan, M. Yazdi, W. Peng, Data–driven–based internal temperature estimation for lithium–Ion battery under variant state–of–charge via electrochemical impedance spectroscopy, Energy Technol. 10 (3) (2022) http://dx.doi.org/10.1002/ente.202100910.

[7] R. Mingant, J. Bernard, V. Sauvant Moynot, A. Delaille, S. Mailley, J.-L. Hognon, F. Huet, EIS measurements for determining the SoC and SoH of Li-ion batteries, ECS Trans. 33 (39) (2011) 41–53, http://dx.doi.org/10.1149/1.3589920.

[8] X. Wang, X. Wei, H. Dai, Q. Wu, State estimation of lithium ion battery based on electrochemical impedance spectroscopy with on-board impedance measurement system, in: 2015 IEEE Vehicle Power and Propulsion Conference, VPPC, IEEE, 2015, pp. 1–5, http://dx.doi.org/10.1109/VPPC.2015.7353021.

[9] Q. Zhang, C.-G. Huang, H. Li, G. Feng, W. Peng, Electrochemical impedance spectroscopy based state-of-health estimation for lithium-ion battery considering temperature and state-of-charge effect, IEEE Trans. Transp. Electrif. 8 (4) (2022) 4633–4645, http://dx.doi.org/10.1109/TTE.2022.3160021.

[10] N. Meddings, M. Heinrich, F. Overney, J.-S. Lee, V. Ruiz, E. Napolitano, S. Seitz, G. Hinds, R. Raccichini, M. Gaberšček, J. Park, Application of electrochemical impedance spectroscopy to commercial Li-ion cells: A review, J. Power Sources 480 (2020) http://dx.doi.org/10.1016/j.jpowsour.2020.228742.

[11] R. Koch, On-line Electrochemical Impedance Spectroscopy for Lithium-Ion Battery Systems: Estimation, Compensation and Avoidance of Measurement Deviations (Ph.D. thesis), Fakultät für Elektrotechnik und Informationstechnik, Technische Universität München, München, 2017.

[12] W. Waag, S. Käbitz, D.U. Sauer, Experimental investigation of the lithium-ion battery impedance characteristic at various conditions and aging states and its influence on the application, Appl. Energy 102 (2013) 885–897, http://dx.doi.org/10.1016/j.apenergy.2012.09.030.

[13] N.S. Spinner, C.T. Love, S.L. Rose-Pehrsson, S.G. Tuttle, Expanding the operational limits of the single-point impedance diagnostic for internal temperature monitoring of lithium-ion batteries, Electrochim. Acta 174 (2015) 488–493, http://dx.doi.org/10.1016/j.electacta.2015.06.003.

[14] P. Keil, Aging of Lithium-Ion Batteries in Electric Vehicles (Ph.D. thesis), Technische Universität München, München, 2017.

[15] T. Landinger, G. Schwarzberger, A. Jossen, A novel method for high frequency battery impedance measurements, in: 2019 IEEE International Symposium on Electromagnetic Compatibility, Signal & Power Integrity, EMC+SIPI, 2019, http://dx.doi.org/10.1109/ISEMC.2019.8825315.

[16] S. Schindler, M.A. Danzer, Influence of cell design on impedance characteristics of cylindrical lithium-ion cells: A model-based assessment from electrode to cell level, J. Energy Storage 12 (2017) 157–166, http://dx.doi.org/10.1016/j.est.2017.05.002.

[17] Y. Troxler, B. Wu, M. Marinescu, V. Yufit, Y. Patel, A.J. Marquis, N.P. Brandon, G.J. Offer, The effect of thermal gradients on the performance of lithium-ion batteries, J. Power Sources 247 (2014) 1018–1025, http://dx.doi.org/10.1016/j.jpowsour.2013.06.084.

[18] S.S. Zhang, K. Xu, T.R. Jow, Electrochemical impedance study on the low temperature of Li-ion batteries, Electrochim. Acta 49 (7) (2004) 1057–1061, http://dx.doi.org/10.1016/j.electacta.2003.10.016.

[19] H. Beelen, L. Raijmakers, M. Donkers, P. Notten, H.J. Bergveld, An improved impedance-based temperature estimation method for Li-ion batteries, IFAC-PapersOnLine 48 (15) (2015) 383–388, http://dx.doi.org/10.1016/j.ifacol.2015.10.055.

[20] H. Beelen, L. Raijmakers, M. Donkers, P. Notten, H.J. Bergveld, A comparison and accuracy analysis of impedance-based temperature estimation methods for Li-ion batteries, Appl. Energy 175 (2016) 128–140, http://dx.doi.org/10.1016/j.apenergy.2016.04.103.

[21] M. Ströbel, V. Kumar, K.P. Birke, Temperature estimation in lithium-ion cells assembled in series-parallel circuits using an artificial neural network based on impedance data, Batteries 9 (9) (2023) 458, http://dx.doi.org/10.3390/batteries9090458.

[22] M. Ströbel, J. Pross-Brakhage, M. Kopp, K.P. Birke, Impedance based temperature estimation of lithium ion cells using artificial neural networks, Batteries 7 (4) (2021) 85, http://dx.doi.org/10.3390/batteries7040085.

[23] J.-q. Li, L. Fang, W. Shi, X. Jin, Layered thermal model with sinusoidal alternate current for cylindrical lithium-ion battery at low temperature, Energy 148 (2018) 247–257, http://dx.doi.org/10.1016/j.energy.2018.01.024.

[24] K. Mc Carthy, H. Gullapalli, T. Kennedy, Real-time internal temperature estimation of commercial Li-ion batteries using online impedance measurements, J. Power Sources 519 (2022) 230786, http://dx.doi.org/10.1016/j.jpowsour.2021.230786.

[25] M. Ranieri, D. Alberto, H. Piret, V. Cattin, Electronic module for the thermal monitoring of a Li-ion battery cell through the electrochemical impedance estimation, Microelectron. Reliab. (2017) http://dx.doi.org/10.1016/j.microrel.2017.06.010.

[26] R.R. Richardson, P.T. Ireland, D.A. Howey, Battery internal temperature estimation by combined impedance and surface temperature measurement, J. Power Sources 265 (2014) 254–261, http://dx.doi.org/10.1016/j.jpowsour.2014.04.129.

[27] R.R. Richardson, S. Zhao, D.A. Howey, On-board monitoring of 2-D spatially-resolved temperatures in cylindrical lithium-ion batteries: Part II. State estimation via impedance-based temperature sensing, J. Power Sources 327 (2016) 726–735, http://dx.doi.org/10.1016/j.jpowsour.2016.06.104.

[28] J.P. Schmidt, S. Arnold, A. Loges, D. Werner, T. Wetzel, E. Ivers-Tiffée, Measurement of the internal cell temperature via impedance: Evaluation and application of a new method, J. Power Sources 243 (2013) 110–117, http://dx.doi.org/10.1016/j.jpowsour.2013.06.013.

[29] L. Wang, D. Lu, M. Song, X. Zhao, G. Li, Instantaneous estimation of internal temperature in lithium–ion battery by impedance measurement, Int. J. Energy Res. 44 (4) (2020) 3082–3097, http://dx.doi.org/10.1002/er.5144.

[30] F. Wenjie, Z. Zhibin, D. Ming, R. Ming, On-line estimation method for internal temperature of lithium-ion battery based on electrochemical impedance spectroscopy, in: 2021 IEEE Electrical Insulation Conference, EIC, IEEE, 2021, pp. 247–251, http://dx.doi.org/10.1109/EIC49891.2021.9612262.

[31] D. Sarkar, R. Bali, T. Sharma, Practical Machine Learning with Python, A Press, Berkeley, CA, 2018, http://dx.doi.org/10.1007/978-1-4842-3207-1.

[32] S. Gantenbein, Impedanzbasierte modellierung von lithium-ionen zellen und deren degradationsverhalten, in: Schriften des Instituts für Angewandte Materialien - Werkstoffe der Elektrotechnik, Karlsruher Institut für Technologie, vol. 39, KIT Scientific Publishing, Karlsruhe, Baden, 2019, http://dx.doi.org/10.5445/KSP/1000099175.

[33] T. Heil, Ersatzschaltbild-basierte Modellierung der Diffusion und des Ladungsdurchtritts in Lithium-Ionen-Zellen (Ph.D. thesis), Technische Universität München, München, 2020.

[34] J. Illig, Physically based Impedance Modelling of Lithium-Ion Cells: Dissertation, Karlsruher Institut für Technologie, Karlsruhe, http://dx.doi.org/10.5445/KSP/1868-1603.

[35] A. Jossen, W. Weydanz, Moderne Akkumulatoren Richtig Einsetzen, second ed., MatrixMedia, Göttingen, 2021, überarbeitete Auflage von März 2019.

[36] L. Liao, P. Zuo, Y. Ma, X. Chen, Y. An, Y. Gao, G. Yin, Effects of temperature on charge/discharge behaviors of LiFePO4 cathode for Li-ion batteries, Electrochim. Acta 60 (2012) 269–273, http://dx.doi.org/10.1016/j.electacta.2011.11.041.

[37] M. Petzl, M. Kasper, M.A. Danzer, Lithium plating in a commercial lithium-ion battery – A low-temperature aging study, J. Power Sources 275 (2015) 799–807, http://dx.doi.org/10.1016/j.jpowsour.2014.11.065.

[38] P. Stein, S. Vollnhals, Grundlagen Clusteranalytischer Verfahren (Ph.D. thesis), Institut fur Soziologie, Universitaet Duisburg-Essen, Duisburg, 2011.

[39] R. Kosfeld, H.F. Eckey, M. Türck, Deskriptive Statistik, Springer Fachmedien Wiesbaden, Wiesbaden, 2016, http://dx.doi.org/10.1007/978-3-658-13640-6.

[40] Samsung SDI, INR21700-50e safety data sheet, 2018, https://files.batteryjunction.com/frontend/files/samsung/msds/SAMSUNG-50E-21700-MSDS.pdf. (Accessed 13 June 2024).

[41] Samsung SDI, INR21700-50e cell specification, 2018, https://e2e.ti.com/cfs-file/_key/communityserver-discussions-components-files/196/INR21700_2D00_50E-Cell-Specification_5F00_V1.0_5F00_180711.pdf. (Accessed 13 June 2024).

[42] R. Srinivasan, Monitoring dynamic thermal behavior of the carbon anode in a lithium-ion cell using a four-probe technique, J. Power Sources 198 (2012) 351–358, http://dx.doi.org/10.1016/j.jpowsour.2011.09.077.

[43] J.G. Zhu, Z.C. Sun, X.Z. Wei, H.F. Dai, A new lithium-ion battery internal temperature on-line estimate method based on electrochemical impedance spectroscopy measurement, J. Power Sources 274 (2015) 990–1004, http://dx.doi.org/10.1016/j.jpowsour.2014.10.182.

[44] R.R. Richardson, D.A. Howey, Sensorless battery internal temperature estimation using a Kalman filter with impedance measurement, IEEE Trans. Sustain. Energy 6 (4) (2015) 1190–1199, http://dx.doi.org/10.1109/TSTE.2015.2420375.

[45] R. Schwarz, K. Semmler, M. Wenger, V.R.H. Lorentz, M. Marz, Sensorless battery cell temperature estimation circuit for enhanced safety in battery systems, in: IECON 2015 - 41st Annual Conference of the IEEE Industrial Electronics Society, IEEE, 2015, http://dx.doi.org/10.1109/IECON.2015.7392319.

[46] L.H.J. Raijmakers, D.L. Danilov, J.P.M. van Lammeren, T.J.G. Lammers, H.J. Bergveld, P.H.L. Notten, Non-zero intercept frequency: An accurate method to determine the integral temperature of Li-ion batteries, IEEE Trans. Ind. Electron. 63 (5) (2016) 3168–3178, http://dx.doi.org/10.1109/TIE.2016.2516961.

[47] P. Haussmann, J. Melbert, Internal cell temperature measurement and thermal modeling of lithium ion cells for automotive applications by means of electrochemical impedance spectroscopy, SAE Int. J. Alternat. Powertrains 6 (2) (2017) 261–270, http://dx.doi.org/10.4271/2017-01-1215.

[48] J. Zhu, Z. Sun, X. Wei, H. Dai, Battery internal temperature estimation for LiFePO4 battery based on impedance phase shift under operating conditions, Energies 10 (1) (2017) 60, http://dx.doi.org/10.3390/en10010060.

[49] H. Beelen, K. Mundaragi Shivakumar, L. Raijmakers, M. Donkers, H.J. Bergveld, Towards impedance–based temperature estimation for Li–ion battery packs, Int. J. Energy Res. 44 (4) (2020) 2889–2908, http://dx.doi.org/10.1002/er.5107.

[50] X. Wang, X. Wei, Q. Chen, J. Zhu, H. Dai, Lithium-ion battery temperature online estimation based on fast impedance calculation, J. Energy Storage 26 (2019) 100952, http://dx.doi.org/10.1016/j.est.2019.100952.

[51] F. Wenjie, Z. Zhibin, D. Ming, R. Ming, On-line estimation method for internal temperature of lithium-ion battery based on electrochemical impedance spectroscopy, in: 2021 IEEE Electrical Insulation Conference, EIC, IEEE, 2021, pp. 247–251, http://dx.doi.org/10.1109/EIC49891.2021.9612262.

[52] X. Du, J. Meng, J. Peng, Y. Zhang, T. Liu, R. Teodorescu, Sensorless temperature estimation of lithium-ion battery based on broadband impedance measurements, IEEE Trans. Power Electron. 37 (9) (2022) 10101–10105, http://dx.doi.org/10.1109/TPEL.2022.3166170.